

AD A100209

(12) **LEVEL II**
AFGL-TR-80-0358
AIR FORCE SURVEYS IN GEOPHYSICS, NO. 424



**The Seismo-Acoustic Disturbance
Produced by a Titan III-D With
Application to the Space Transportation System
Launch Environment at Vandenberg AFB**

FRANCIS A. CROWLEY
EUGENE B. HARTNETT
HENRY A. OSSING

17 November 1980



Approved for public release; distribution unlimited.

DTIC FILE COPY

TERRESTRIAL SCIENCES DIVISION PROJECT 7600
AIR FORCE GEOPHYSICS LABORATORY
HANSCOM AFB, MASSACHUSETTS 01731

AIR FORCE SYSTEMS COMMAND, USAF

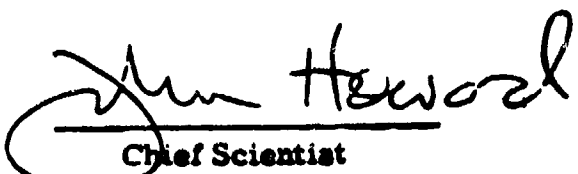


21 6 15 179

This report has been reviewed by the ESD Information Office (OI) and is releasable to the National Technical Information Service (NTIS).

This technical report has been reviewed and is approved for publication.

FOR THE COMMANDER


John Haworth
Chief Scientist

Qualified requestors may obtain additional copies from the Defense Technical Information Center. All others should apply to the National Technical Information Service.

(14) AFGL-TR-80-0358
AFGL-TR-AFSG-434

Unclassified

SECURITY CLASSIFICATION OF THIS PAGE (When Data Entered)

REPORT DOCUMENTATION PAGE		READ INSTRUCTIONS BEFORE COMPLETING FORM
1 REPORT NUMBER	2 GOVT ACCESSION NO.	3 RECIPIENT'S CATALOG NUMBER
AFGL-TR-80-0358	AJ-A100209	
4 TITLE (Include classification) <u>THE SEISMO-ACOUSTIC DISTURBANCE PRODUCED BY A TITAN III-D WITH APPLICATION TO THE SPACE TRANSPORTATION SYSTEM LAUNCH ENVIRONMENT AT VANDENBERG AFB</u>		5 TYPE OF REPORT & PERIOD COVERED Scientific, Interim.
6 PERFORMING ORG. REPORT NUMBER AFSG No. 434		7 CONTRACT OR GRANT NUMBER(S)
8 PERFORMANCE PERIOD NAME AND ADDRESS Air Force Geophysics Laboratory (LW) Hanscom AFB Massachusetts 01731		9 PROGRAM ELEMENT PROJECT TASK AREA & WORK UNIT NUMBERS 62101F 76000903
10 CONTROLLING OFFICE NAME AND ADDRESS Air Force Geophysics Laboratory (LW) Hanscom AFB Massachusetts 01731		11 12 MONTH DAY 11 17 November 1980
12 MONITORING AGENCY NAME & ADDRESS (if different from Controlling Office) 12 73		13 NUMBER OF PAGES 74
14 DISTRIBUTION STATEMENT (or this Report)		15 SECURITY CLASS (of this report) Unclassified
16 DISTRIBUTION STATEMENT (for the contract entered in Block 10, if different from Report)		17 DECLASSIFICATION/DOWNGRADING SCHEDULE
18 SUPPLEMENTARY NOTES *Boston College		
19 KEY WORDS (Continue on reverse side if necessary and identify by block number) Rocket plume acoustics Vibro-acoustic effects Air-coupled waves		
20 ABSTRACT (Continue on reverse side if necessary and identify by block number) A vibro-acoustic study of a Titan III-D rocket launch was conducted at Vandenberg AFB for the purpose of predicting the seismic and acoustic fields for future Space Transportation System launches. The resulting vibro-acoustic forecasts are configured to permit vibration estimates within critical STS ground facilities. It was determined that rocket-induced ground motion is dominated by the complex branch of the air-coupled wave, and that the surface pressure travels as a nondispersive, spatially coherent acoustic load over the distances and frequencies of concern.		

DD FORM 1 JAN 73 EDITION OF 1 NOV 65 IS OBSOLETE

Unclassified

SECURITY CLASSIFICATION OF THIS PAGE (When Data Entered)

409578

Approved for	NTIS GR&I
LFB 5/8	<input checked="" type="checkbox"/>
Distribution	<input type="checkbox"/>
Justification	
By	
Distribution/	
Availability Codes	
Dist	Avail and/or Special
<i>A</i>	

Contents

1. INTRODUCTION	7
1.1 Purpose	7
1.2 Approach	7
1.3 Summary of Findings	8
2. PHYSICAL CONSIDERATIONS	8
2.1 Empirical	8
2.2 Theoretical	9
2.2.1 Plane Wave Acoustic Excitation of a Layer	9
2.2.2 Concentrated Source	12
2.3 Prediction	14
3. MEASUREMENTS	14
3.1 System Response	14
3.2 Protection Ratios	15
3.3 Measurement Noise	17
4. OBSERVATIONS	19
4.1 Introduction	19
4.2 Ignition Pulse	20
4.2.1 Velocity Estimate	22
4.2.2 Attenuation Estimate	22
4.3 Admittance	22
4.3.1 Measurement	22
4.3.2 Prediction	25
4.4 Plume Emitted Acoustics	25
4.4.1 Time Averaging	25
4.4.2 Plume Emitted Surface Pressure	27
4.4.3 Phase Velocity	31
4.4.4 Coherence	32
4.4.5 Spectral Estimates	35

Contents

5. ADMITTANCE ESTIMATES	41
6. SCALING TITAN III-D INTO STS	44
6.1 Power Spectra Density Estimates	44
6.2 OBSPL Estimates	46
7. GROUND RESPONSE AT SLC-6	50
REFERENCES	55
LIST OF SYMBOLS AND ABBREVIATIONS	57
APPENDIX A: Computerized Algorithm for a Layered Whole Space	59
APPENDIX B: Inverse Operator	65
APPENDIX C: Admittance Estimate and Prediction Operator	67
APPENDIX D: Titan III Launch Profile	69
APPENDIX E: Phase Velocity and Azimuth Estimate	73

Illustrations

1. Alluvial Layer Model	10
2. Admittance Magnitude: Air Alluvial Interface Model	11
3. Layer Response	12
4. Ratio of Surface Pressure to Incident Pressure	13
5. Air-Coupled Rayleigh Wave	13
6. Vibro-Acoustic Array	15
7. Pressure Channel Amplitude Response	16
8. Seismic Channel Amplitude Response	16
9. First Fold Protection Ratio: Pressure Channels	17
10. Noise Spectral Estimate: Pressure	18
11. Noise Spectral Estimate: Seismic	19
12. Observed Component Motions: Titan III-D Source	20
13. Ignition Pulse Wavelet	21
14. Optimum Delay Estimates	23
15. Optimum Attenuation Factors	23
16. Bandpass RMS Surface Pressure	24
17. Observed Ground Admittance	24

Illustrations

18. Predicted/Measured Ground Motions: Titan III-D	26
19. Relative Ground Motion Prediction Error	26
20. Broadband RMS Surface Pressure	28
21. Rocket Source Geometry	28
22. Amplitude Ratio During Peak Loading	30
23. Phase Velocity During Peak Loading	30
24. Residual Error for Maximum Loading	31
25. Estimated Phase Velocity vs. Time	32
26. Phase Velocity: 8.7 sec After Launch	33
27. Runs Test for Dispersion	33
28. Coherency Estimate	34
29. Spacial Coherence	34
30. Observed Spectra	36
31. Peak Load Spectral Estimates	36
32. Spectral Estimates: 8.51 sec After Ignition	38
33. Theoretical Test Statistics Acceptance Test	38
34. Overall Sound Power Level	40
35. Frequency at the Spectral Maximum	40
36a. Measured Admittance: Fundamental	41
36b. Measured Admittance: First Mode	42
37a. Admittance Maxima: Fundamental	42
37b. Admittance Maxima: First Mode	42
38. Apparent Directivity	43
39. Radiation Pattern from Phase Velocity	44
40. Titan Spectra in Standard Form	45
41. Acoustic Surface Pressure around Maxima Loading	47
42. STS Surface Spectra	47
43. STS OBSPL Estimates: () 2.56 sec	49
44. Effect of Averaging Time	49
45. STS Estimates OBSPL: () 0.3 sec	50
46. Ground Admittance near LCC, SLC-6	51
47. LCC Basement Response	52
48. Ground Level Amplitude Ratio: LCC Base Run	52
D1. Launch Profile	71

Tables

1. Overall Sound Power Values	39
2. Rocket Engine Parameters	45
3. Overall Sound Pressure Levels	48
D1. Titan III Launch Profile Values	70

**The Seismo-Acoustic Disturbance
Produced by a Titan III-D
With Application to the Space Transportation
System Launch Environment at Vandenberg AFB**

1. INTRODUCTION

1.1 Purpose

This study was conducted in an effort to forecast the seismic and acoustic fields for Space Transportation System (STS) launches at Vandenberg Air Force Base (VAFB) in a form that permits vibration estimates within critical STS ground facilities (abbreviations used in this report are contained in the List of Abbreviations following the text).

1.2 Approach

With SAMSO support, AFGL undertook the following items of work to develop a technology base for predicting motion due to STS operations at Space Launch Complex 6 (SLC 6), VAFB.¹

1. From physical considerations, identify those properties of the launch pressure field needed to predict ground motion.
2. Measure the acoustic load developed by a large class chemical rocket in a manner needed for making ground motion and facility vibration forecasts.

(Received for publication 14 November 1980)

1. SAMSO/AFGL Memorandum of Agreement, dated 31 January 1979.

3. Forecast those properties of the acoustic load due to a STS launch needed for ground motion and facility vibration estimates.
4. Determine the ground response at SLC-6 to a coherent acoustic load over a path of interest.
5. Predict the ground motion in the general area of the Launch Control Center (LCC) for a STS launch at SLC-6.

1.3 Summary of Findings

Our observations indicate that the surface pressure developed during a Titan III-D launch travels largely as a nondispersive, spacially coherent acoustic load over the distances and frequencies of concern. Also, the "accepted" directivity index, based on extrapolating pressure levels, differs markedly from the plume radiation pattern based on phase velocity. This study also determined that the motion of the ground, excited by a rocket launch, is dominated by the complex branch of the so-called "air-coupled" wave.

An admittance term obtained from small atmospheric explosions is used to predict motion at SLC-6 for a STS launch. The predicted motion is sensitive to our forecast of the pressure level, phase velocity and spacial coherency of the acoustic load generated by the STS plume over the path, time and frequencies of interest.

2. PHYSICAL CONSIDERATIONS

2.1 Empirical

Ground motion excited by a rocket launch travels outward along one of two paths. The first path runs directly through the ground from the stressed zone in the immediate vicinity of the launch pad. The second and more important path is determined by coupling the acoustic load into the ground along the travel path.

Commonly, the large density contrast between the air and ground effectively decouples the acoustic and seismic regimes. The normal acoustic impedance Z , defined by the amplitude ratio of the surface pressure to the ground's vertical particle velocity, typically is very large.²

$$Z(c, f, z = 0) = p(c, f)/V(c, f) \quad \text{LARGE}$$

2. Morse, P., and Feshbach, H. (1953) Methods of Theoretical Physics, Part II, McGraw-Hill, New York.

Conversely, the reciprocal of impedance, admittance, is quite small.

$$Z(c, f, z = 0)^{-1} = Y(c, f) \approx V/p$$

For the usual condition, the ground behaves nearly as a rigid body to acoustic inputs. The incident pressure $p(c, f)$ is completely reflected without a phase change, and the surface pressure, $p_s(c, f, z = 0)$ is double the incident pressure.

$$p_s(c, f, 0) = p_i + p_r = 2p_i$$

Measurements of rocket launches at the NASA Kennedy Space Center by Mickey³ and McCarty and Dalins⁴ show the seismic disturbance coming directly through the ground from the launch zone to be negligible compared to the seismics following the acoustic arrival. We also find this to be true for our observations at VAFB; ground motion prior to the acoustic arrival, carried directly by the high speed seismic ground path, is small. As at the Kennedy Space Center, rocket launch generated seismics are due to acoustically excited ground resonances whose characteristics are determined by the elastic properties, densities, and layering of the geological section surrounding the launch area. The ground structure both at SLC-4 and SLC-6 is also of a kind that supports "air-coupled" seismic waves.

2.2 Theoretical

2.2.1 PLANE WAVE ACOUSTIC EXCITATION OF A LAYER

Insights about the relation between surface pressure and ground motion can be developed by considering the motion of a low speed "alluvial" layer sandwiched between "atmospheric" and "rock" half-spaces in the manner of Figure 1. As shown, we excited the model from above by a homogeneous acoustic plane wave of frequency f , phase velocity c , and pressure amplitude p .

Modifying the formulation of Haskell⁵ and the computational algorithm of Abo-Zena⁶ for a layered half-space (Appendix A), we compute the magnitude of

3. Mickey, W. (1962) Seismic Investigation of Missile Launchings, U.S. Dept. of Commerce, Coast and Geodetic Survey Publication.
4. McCarty, V., and Dalins, I. (1974) Frequency shift in air-coupled surface waves originated by rocket launches, J. Geophys. Res. 76:7027-7039.
5. Haskell, N. (1962) Crustal reflection of P and SV waves, Bull. Seism. Soc. Am. 52:4751-4767.
6. Abo-Zena, A. (1979) Dispersion function computations for unlimited frequency values, Geophys. J. R. Astr. Soc. 58:91-105.

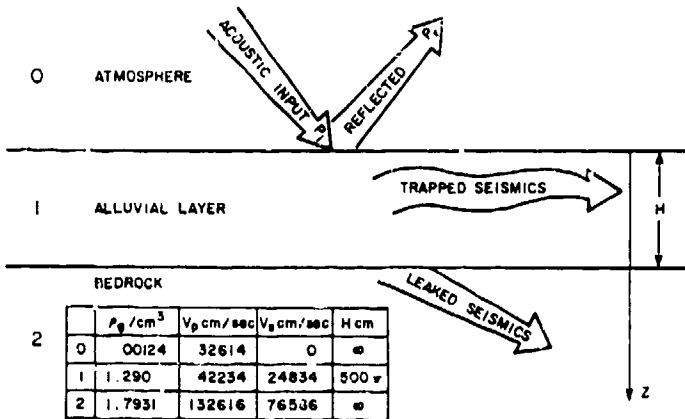


Figure 1. Alluvial Layer Model

the admittance at the "air-alluvial" interface for an acoustic input near grazing incidence $c \approx c_\alpha'$, as seen in Figure 2. We choose to compute admittance here, for it is in harmony with our concept of the response of a linear elastic system to an "input pressure" that excites an "output particle velocity." In Figure 2, the magnitude of admittance, the amplitude ratio of the vertical particle velocity to surface pressure, is given as a function of frequency for the model. As depicted, the magnitude is quite small for all but a subset of frequencies, the so-called "air-coupled" frequencies.⁷ The value of admittance and the location of the air-coupled frequency is sensitive to the elastic parameters, layer thickness as well as the phase velocity of the acoustic load.^{7,8}

We now locate large admittance values of our model as they relate to the phase velocity and frequency of the acoustic input. The loci of high response values are found to cluster along various modal lines under this mapping. For phase velocities $c_R \leq c \leq c_\alpha'$, the loci of high responses coincide with the locked normal modes; that is, the inhomogeneous Rayleigh waves characteristic of a free surface layer.⁷ For $c > c_\alpha'$, the alluvial layer behaves like a leaky wave guide.^{7,9}

-
- 7. Ewing, W., et al (1957) Elastic Waves in a Layered Media, McGraw-Hill, New York.
 - 8. Crowley, F., and Ossing, H. (1969) On the Application of Air-Coupled Seismic Waves, AFCRL-69-0312.
 - 9. Gilbert, F. (1964) Propagation of transient leaking modes in a stratified elastic waveguide, Reviews of Geophysics 3:123-153.

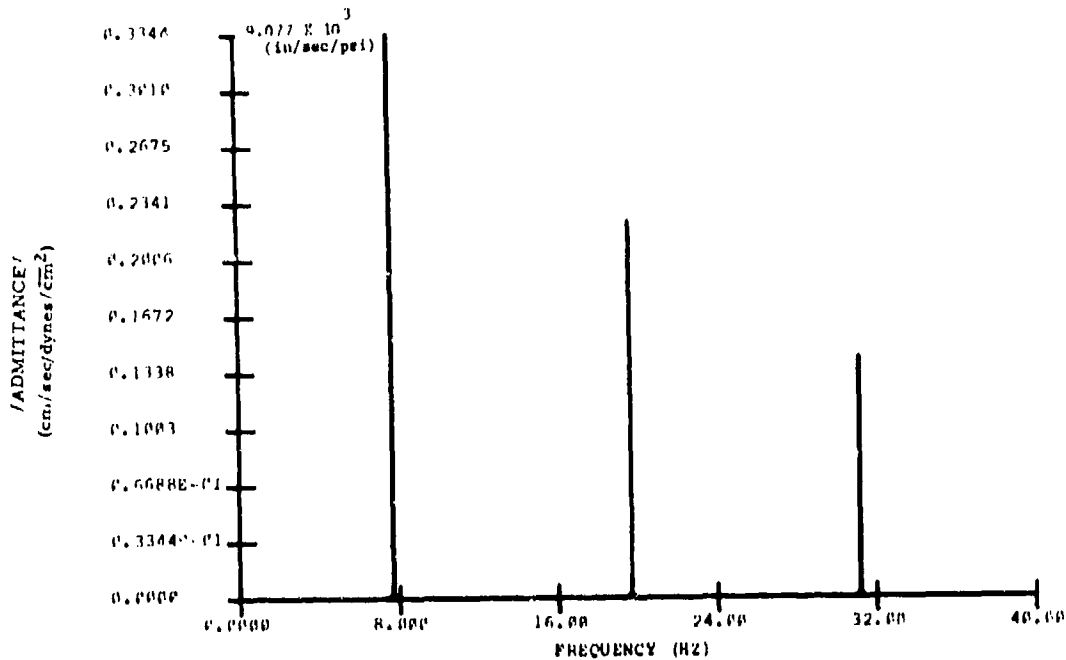


Figure 2. Admittance Magnitude: Air Alluvial Interface Model

As can be seen in Figure 3, large admittance values generally migrate toward smaller frequency values for increasing phase velocity. Looking ahead to the ground motion excited by a rocket launch, we can anticipate that the frequency of air-coupling will also migrate as the phase velocity of the incident acoustic wave excited by the rocket changes with time.

Attributes of the air-coupled phase have been discussed at length in the seismic literature.^{10, 11} In particular, the phenomena of surface pressure at Rayleigh velocities has been considered both by Haskell¹² and Gubanov.¹³ To show the relation, we now compute the ratio of surface pressure to incident pressure for our model for $c \approx c_\alpha$. Here we find the computed value of surface pressure to be quite close to double the incident source pressure almost

-
- 10. Donn, W., et al (1971) Air-coupled seismic waves at long range from Apollo launchings, J. R. Astr. Soc. 26:161-171.
 - 11. Espriosa, A., and Mickey, W. (1968) Observations of coupled seismic waves from sonic booms, a short note, Acustica 20:88-91.
 - 12. Haskell, N. (1951) A note on air-coupled surface waves, Bull. Seism. Soc. Am. 41:295-300.
 - 13. Gubanov, A. (1945) Rayleigh waves on a boundary between a solid and a liquid, J. Exptl. Theoret. Phys. (USSR) 15:497.

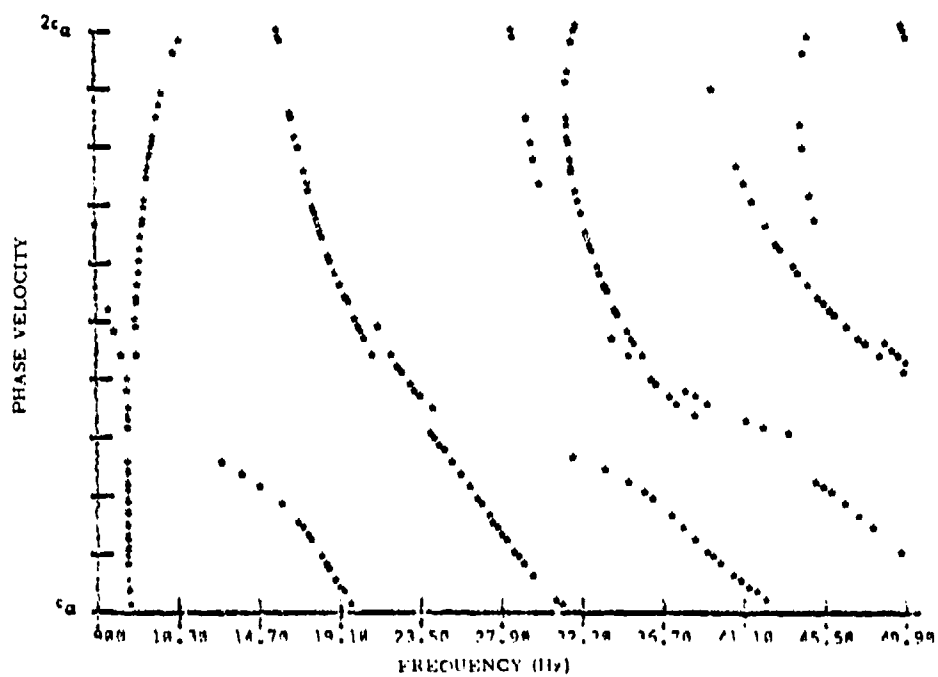


Figure 3. Layer Response

everywhere in the manner of a rigid earth, except at the air-coupled frequencies (see Figure 4). At the air-coupled frequencies, the reflected acoustic wave is π out of phase with the incident term; the surface pressure approaches zero. In our model we find that the relation between surface pressure and free field pressure is a sensitive function of the model's geologic parameters. High resolution surface acoustic spectra also should be site sensitive.

2.2.2 CONCENTRATED SOURCE

The phenomenon of the air-coupled phase excited by a concentrated pressure source has been considered by Ewing et al⁷ as an extension of Rayleigh wave propagation in a layered half-space. After Ewing (see Figure 5), we find the fundamental air-coupled phase trails the sound wave as an almost constant frequency vibration with a duration T given by

$$T = \Delta(1/c_0 - 1/U_0)$$

where c_0 , U_0 , are the phase and group velocities of the half-space model at the air-coupled frequency. As shown in Figure 5, the dotted line depicts the departure in the normal mode response of the half-space model due to the atmosphere. For

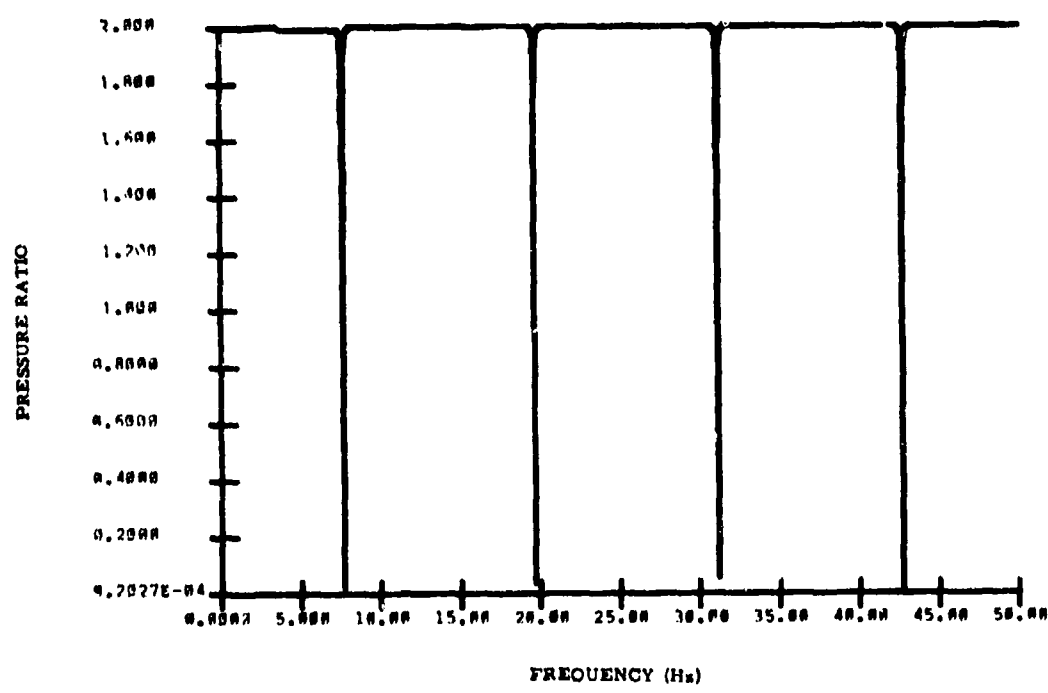


Figure 4. Ratio of Surface Pressure to Incident Pressure

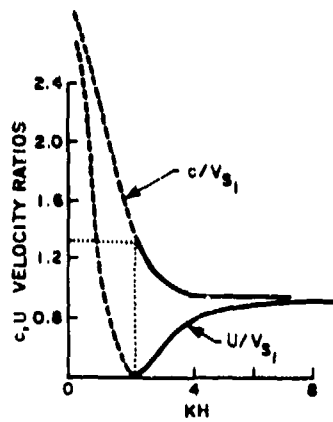


Figure 5. Air-Coupled Rayleigh Wave

phase velocities around the speed of sound in air, the layer response couples at the half-space Rayleigh wave. For phase velocities above c_a , the modal response is diminished by leakage. Since bandwidth inversely depends on duration, we can also anticipate that the bandwidth of the air-coupled phase will be inversely related to the distance to the source. In practice we find that the bandwidth, or equivalently the duration of the air-coupled phase, depends more on the uniformity and extent of the layering neighboring the observer.⁸

2.3 Prediction

From both model calculations and field measurements, we find that a surficial layer having the density and elastic constants typical of unconsolidated sediments substantially alters the "usual" dense earth relation between the free field pressure and surface pressure as well as the relation between surface pressure and ground motion. The ground response due to a propagating acoustic load can be quite intense around the "air-coupled" frequencies. For the usual condition of a low velocity unconsolidated layer overlying a high speed rock, the frequency of the "air-coupled" phase tends to migrate to lower frequencies and smaller absolute values at higher phase velocities.

Given an input acoustic pressure, the output ground motion can be forecast through admittance. For a uniform area, the admittance can be computed once the elastic properties, densities, and layer thicknesses are known. For an area of unknown or complicated structure, the admittance over any given path can be measured. We take the latter approach, namely premeasure the admittance over a path of interest.

In order to forecast seismic motion due to an STS launch at SLC-6, VAFB, through ground admittance, we must first establish the intensity, frequency, phase velocity, and spacial coherency of the acoustic load expected for a STS launch. We attempt this by extrapolating measured values found for a large class chemical rocket (Titan III-D) to corresponding terms governing the acoustic load expected for a STS launch.

3. MEASUREMENTS

3.1 System Response

The location of the AFGL sensors used to characterize the acoustic load generated by a Titan III-D rocket is given in Figure 6. The sensor array consists of nine low range pressure transducers and seven seismometers. Factory calibrations for the pressure sensors were certified at AFGL; the seismic elements were calibrated in place at the launch complex. The array was located along a

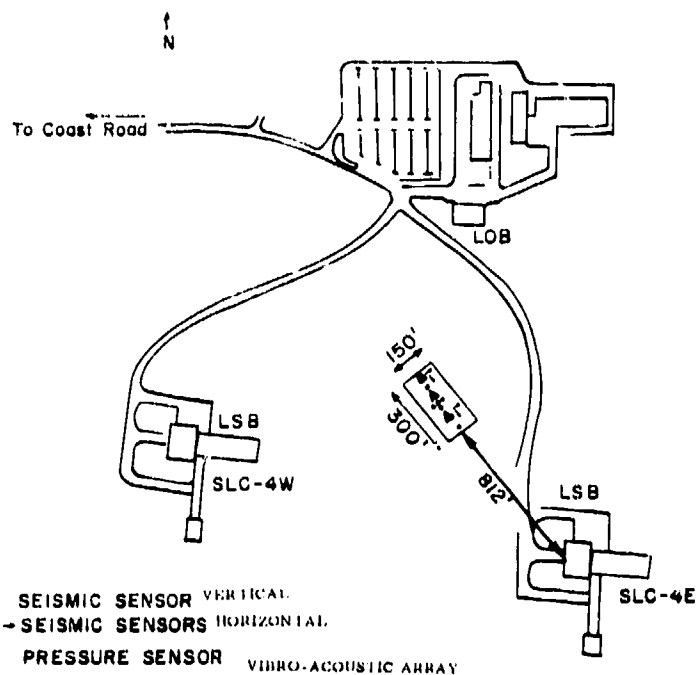


Figure 6. Vibro-Acoustic Array

strip northwest of the SLC-4E launch pad. The array's dimensions and location were set by the distance to and size of critical STS support facilities at SLC-6. The pressure sensors were located on the surface; the seismometers were buried in shallow holes.

The output of each of the 16 sensors was amplified and transmitted to a data acquisition system located in the Launch Operations Building (LOB). Here the observations were digitized at a 100 samples per second rate and stored on magnetic tape for later retrieval and analysis. The period of measurement started 1 min before ignition and continued to 20 min.

The design response of a pressure channel is shown in Figure 7; the corresponding response for seismic measurements is given in Figure 8.

3.2 Protection Ratios

Since the data were digitized at a 100 sample rate, our measurement band is limited to something less than 50 Hz. An estimate of the useful measurement band can be calculated from the ambient noise figure and the amplitude protection ratio.

The first fold protection ratio for the pressure data, defined by the ratio of the amplitude response at the measurement frequency to the corresponding

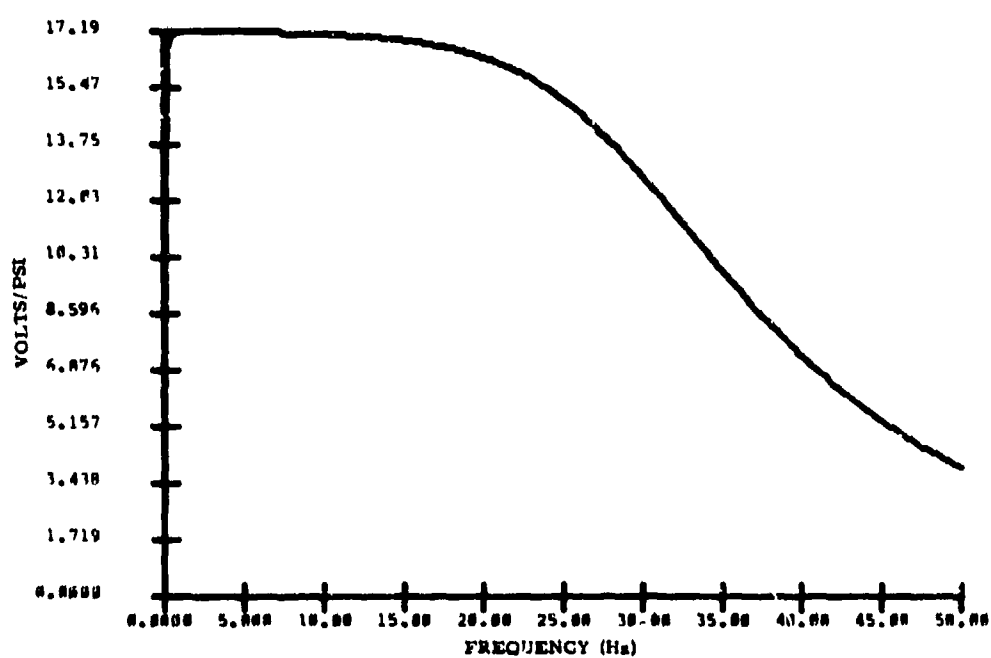


Figure 7. Pressure Channel Amplitude Response

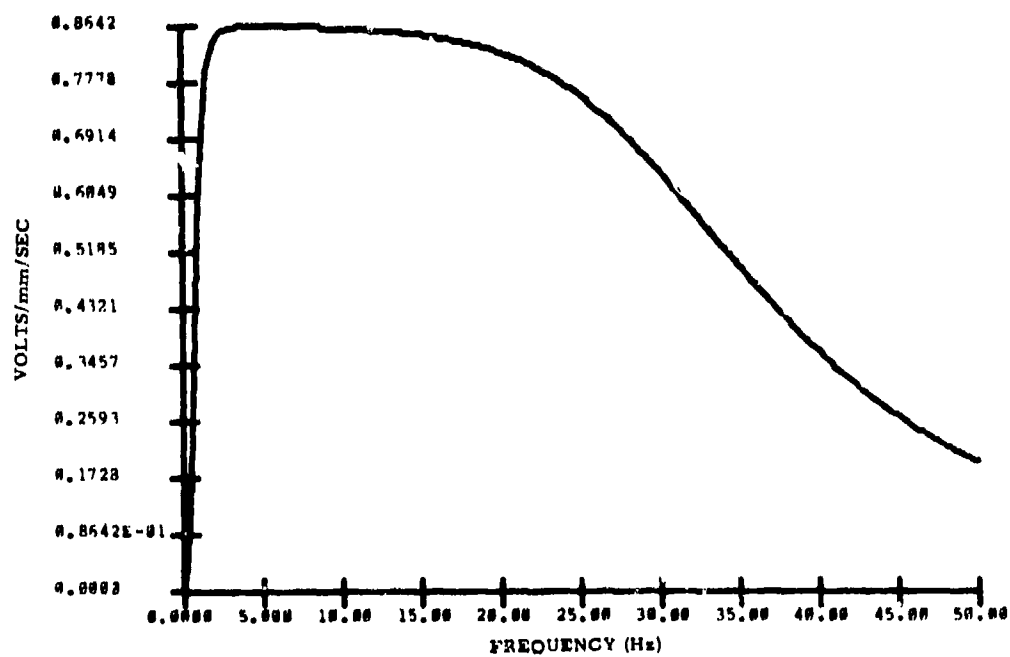


Figure 8. Seismic Channel Amplitude Response

response at the first fold alias of that frequency,¹⁴ is given in Figure 9. The design protection ratios for the seismic and pressure channels are quite similar. The reason for this similarity is elementary; the signal and noise characteristics for both pressure and seismic measurements above our midband frequency are similar. Above 25 Hz both the pressure and seismic inputs rolloff at 6 db per octave. For a midband measurement, we anticipate that the "effective" protection ratio, determined by the ratio of the actual value of the measurement inband to the corresponding aliared term, is about three times better than that shown in Figure 9.

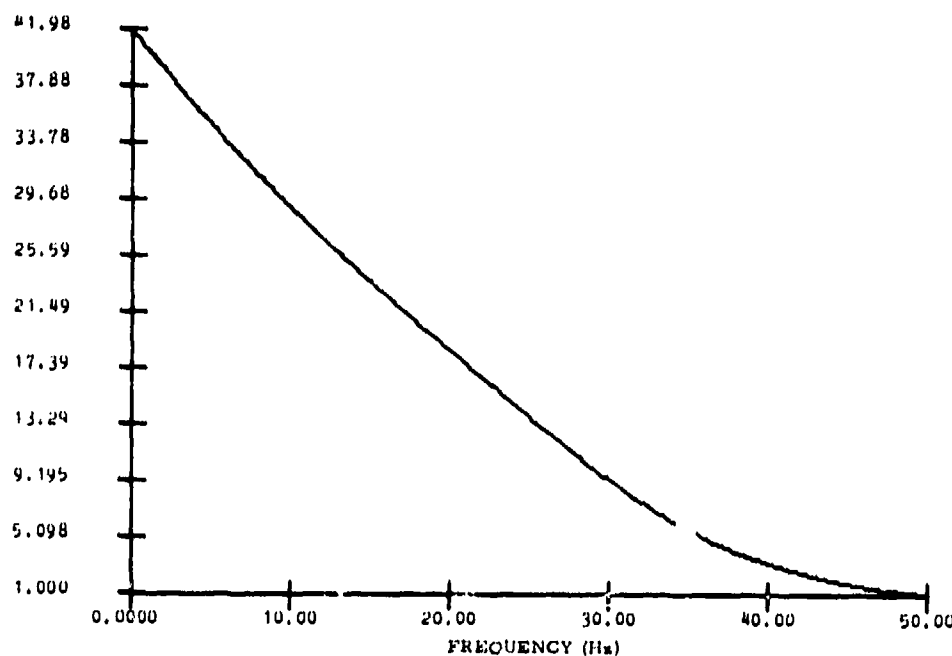


Figure 9. First Fold Protection Ratio: Pressure Channels

3.3 Measurement Noise

Our estimate of measurement noise is based on seismic and pressure observations taken 1 min before ignition. We treat these data to be from a stationary random process that is uncorrelated and additive to the launch signal. Under these assumptions the noise and signal spectra will simply add.

14. Blackman, R. and Tukey, W. (1959) The Measurement of Power Spectra, Dover Publications, New York.

The ambient noise spectral estimates given here are based on the Discrete Fourier Transform (DFT's) averaged over twenty 2.56-sec measurement intervals. The variance of the averaged unweighted periodogram estimates is about 5 percent of the square of the spectra of the idealized process.¹⁵ Hanned measurement noise spectral estimates, referred to the input, are given in Figure 10 and Figure 11. The variance of these estimates is expected to be about 40 percent of that of the unweighted form.

The ambient noise value given here is a composite of ambient pressure or ground motion as well as amplifier, cable and digitization noise. In our passband (1-30 Hz), the RMS total noise figure for the seismic channels is 1.25×10^{-2} mm/sec; the corresponding term for the pressure measurements is 6.5×10^{-4} psi (1.9×10^{-3} kg/cm²). It should also be recognized that the low frequency limb of the pressure spectra is very sensitive to wind speed at the time of measurement. After Kimball,¹⁶ we can anticipate a 50-fold increase in the surface pressure spectra for a 2-fold increase in wind speed. A nonacoustic pressure term, due to launch induced turbulence, can be anticipated at low frequencies.

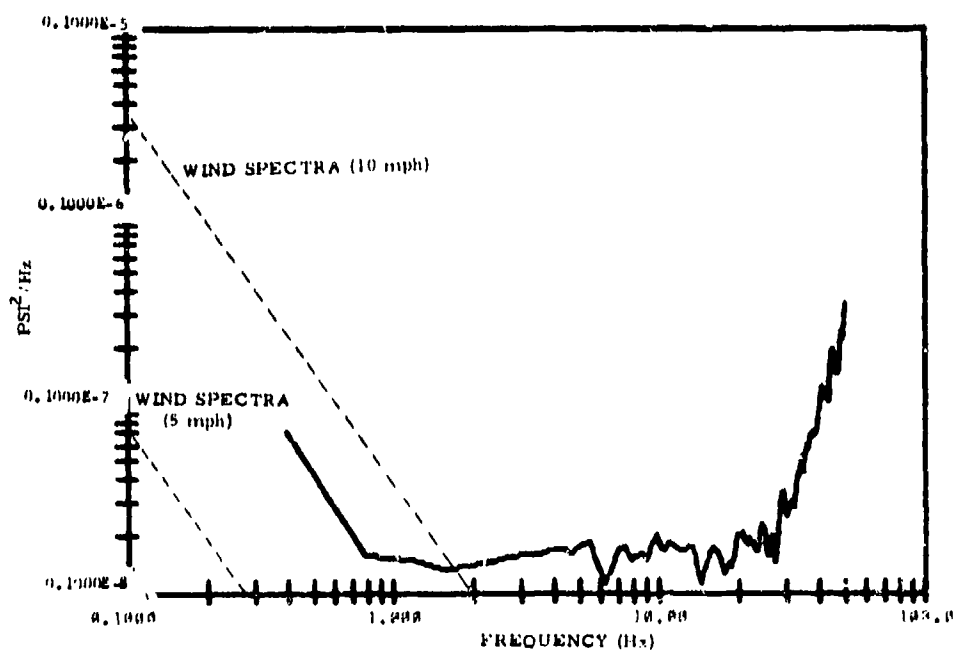


Figure 10. Noise Spectral Estimate: Pressure

The references cited above will not be listed here. See References, page 55.

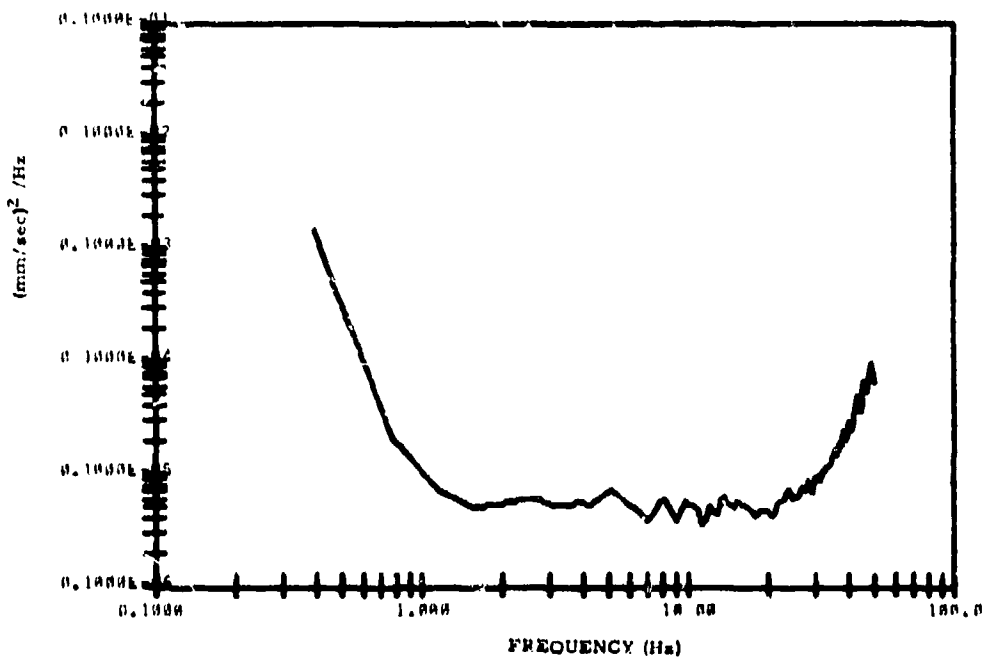


Figure 11. Noise Spectral Estimate: Seismic

4. OBSERVATIONS

4.1 Introduction

The surface pressure, as well as the vertical, radial, and transverse seismic motion caused by the Titan III-D launch of 16 March 1979, is shown in Figure 12 for an observation point 890 ft (271 m) northwest of SLC-4E. The data shown here are corrected for our system response in that the effect of the system response on the observations is suppressed by linear deconvolution. The inversion operators used here are extended until they recover the expected input with a mean square error of less than 0.1 percent (Appendix B).

As can be seen, the duration of the significant disturbance is less than half a minute. The launch signals start abruptly with an "ignition pulse" that is followed by a buildup in level that reaches a maximum intensity in about 9 sec. Following this maximum, the plume generated surface pressure level trails off in exponential fashion. As at Cape Kennedy, we find that conspicuous ground motion follows the acoustic arrival. The envelope of the seismic motion roughly mirrors that of the pressure. Also, the motion intensity level is pretty much the

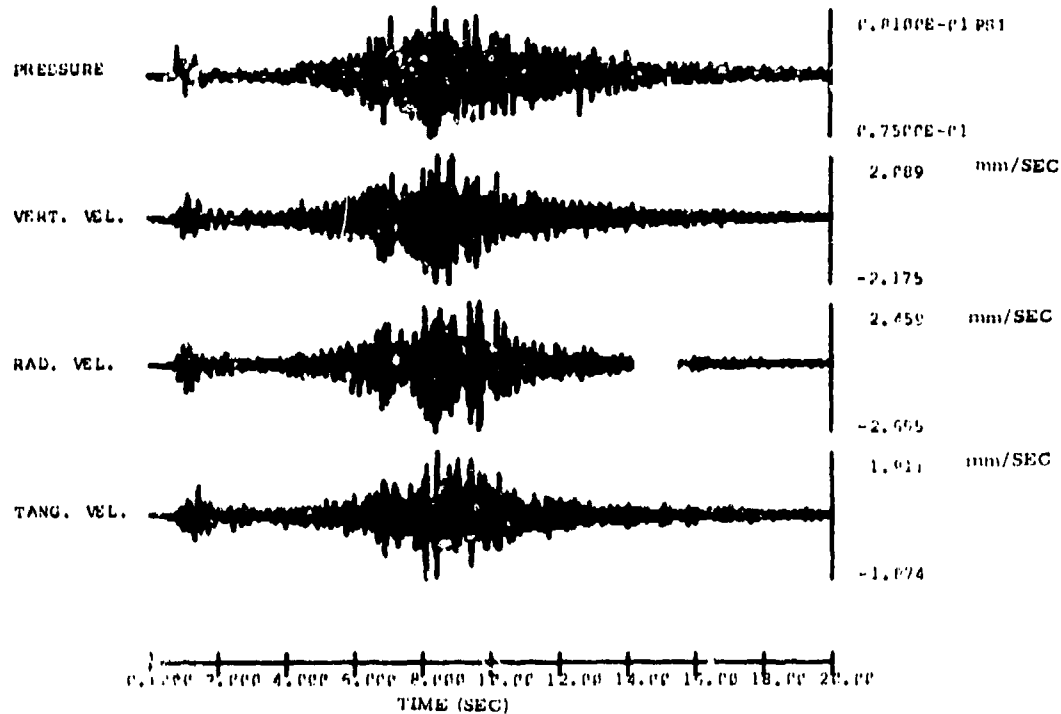


Figure 12. Observed Component Motions: Titan III-D Source

same on each ground component. This unexpected result is in harmony with like ground measurements at Kennedy.¹⁷

4.2 Ignition Pulse

The observed ignition pulse can be represented as a propagating wavelet of something less than 2 sec duration (Figure 13) with an attenuation factor $(\Delta_j/\Delta_o)^{-n}$ independent of wave number, and a propagation delay, $(\Delta_j - \Delta_o)/c$ independent of frequency:

$$p'(\Delta_j, t) = (\Delta_j/\Delta_o)^{-n} p(\Delta_o, t_o - (\Delta_j - \Delta_o)/c) . \quad (1)$$

17. Ballard, R. (1970) Dynamic Behavior of Launch Facility Foundation and Surrounding Areas, Miscellaneous Paper S-70-20, U.S. Army Waterways Experimental Station.

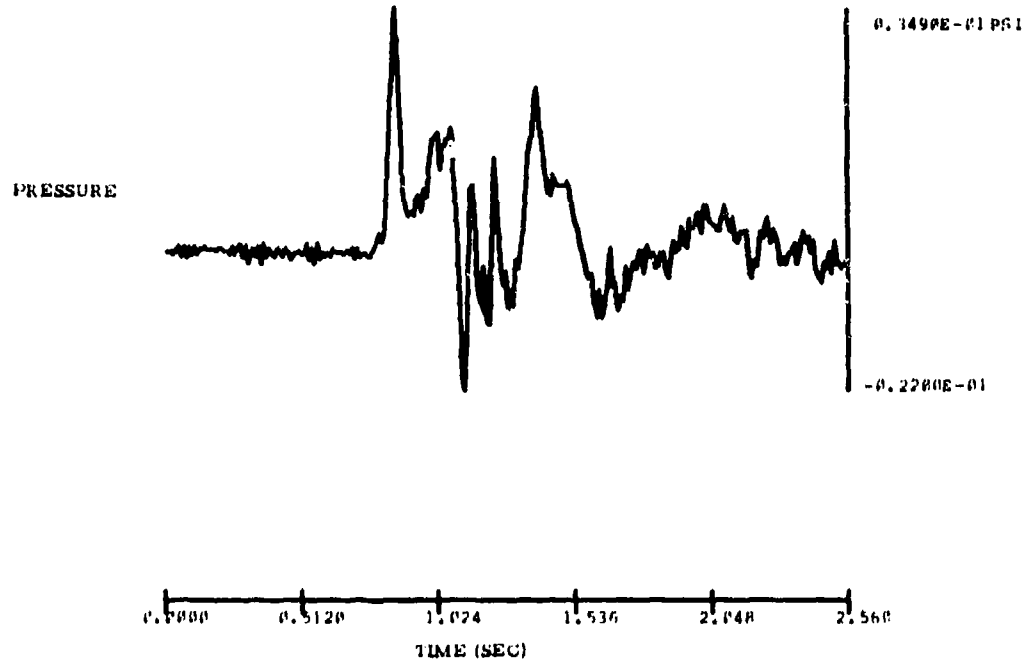


Figure 13. Ignition Pulse Wavelet

A best estimate of attenuation and delay $[(\Delta_j/\Delta_0)^{-1}(\Delta_j - \Delta_0)/c]$ is defined to be the (\hat{n}, \hat{c}) pair that minimizes the sum square difference between the measured and predicted pressure values, namely

$$\frac{1}{n-1} \sum_{i=1}^n (p(\Delta_j, t_i) - p^*(\Delta_j, t_i))^2 = \langle \epsilon_j^2 \rangle_{\min} \quad (2)$$

In turn, a figure of merit M is formed to test the representation:

$$M_j \% = [1 - \langle \epsilon_j^2 \rangle / S_0^2] \quad ,$$

where S_0^2 is the mean square of the measured pressure wavelet found at Δ_0 in excess of the additive ambient noise existing just prior to launch.

4.2.1 VELOCITY ESTIMATE

Figure 14 is a plot of the best delay estimates, as they relate to separation ($\Delta_j - \Delta_0$). The phase delay times computed here are given to a precision that is one order of magnitude higher than 0.01 sec of the field measurements. This is done by taking advantage of the shift properties of the Fast Fourier Transform,¹⁸ namely

$$p(\Delta_j, t - \tau_j) = \text{FFT}^{-1}[\text{FFT}(p(\Delta_j, t)) \cdot e^{tj\omega T}] .$$

The velocity of propagation for the ignition wavelet based on our τ estimates is 1102 ft/sec (335.9 m/sec), the speed of sound in air for the wind and temperature conditions prevailing at launch time.

4.2.2 ATTENUATION ESTIMATE

The log of best attenuation factors is given in Figure 15 as they relate to the source distance. The attenuation exponent found here lies midway between the attenuation of a point and line source in a homogeneous whole space.² Clearly, the attenuation is significantly less than the $(1/\Delta)$ term often used to adjust pressure estimates.^{19, 20}

Figure 16 summarizes the residual error for our representation as it relates to separation. The mismatch between the observed and predicted ignition wavelet pressures leaves a residual error of slightly more than 1 percent. Our representation of the ignition pressure wavelet, as given in Eq. (1), is found to be quite insensitive to separation. Over the range of our measurements the ignition surface pressure wavelet propagates coherently and nondispersively (without a change in form) at the speed of sound in air with an attenuation factor that is somewhat less than that ascribable to a spherical divergent wavefront.

4.3 Admittance

4.3.1 MEASUREMENT

We now use the ignition wavelet to establish the admittance for a near surface pressure source exciting the ground over our measurement path (see Figure 17):

$$Y(c_a, f) .$$

-
18. Oppenheim, A., and Schafer, R. (1975) Digital Signal Processing, Prentice-Hall, N.J.
 19. Cole, J. et al (1957) Noise Radiation from Fourteen Types of Rockets in the 1,000 to 130,000 Pounds Thrust Range, WADC Technical Report 57-354, (AD 130 794).
 20. NASA Report Sp-8072 (1971) Acoustic Loads Generated by the Propulsion System.

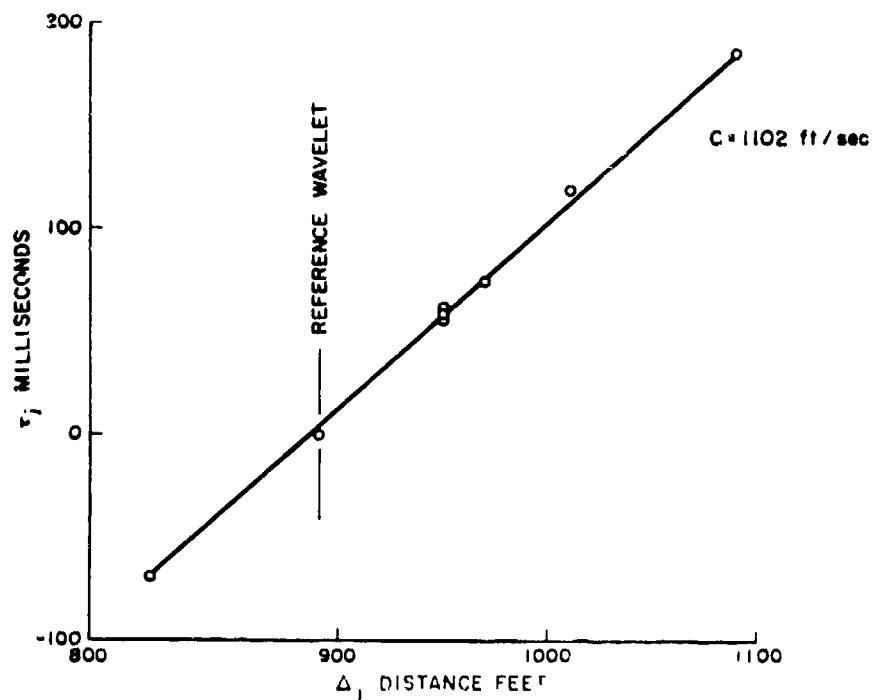


Figure 14. Optimum Delay Estimates

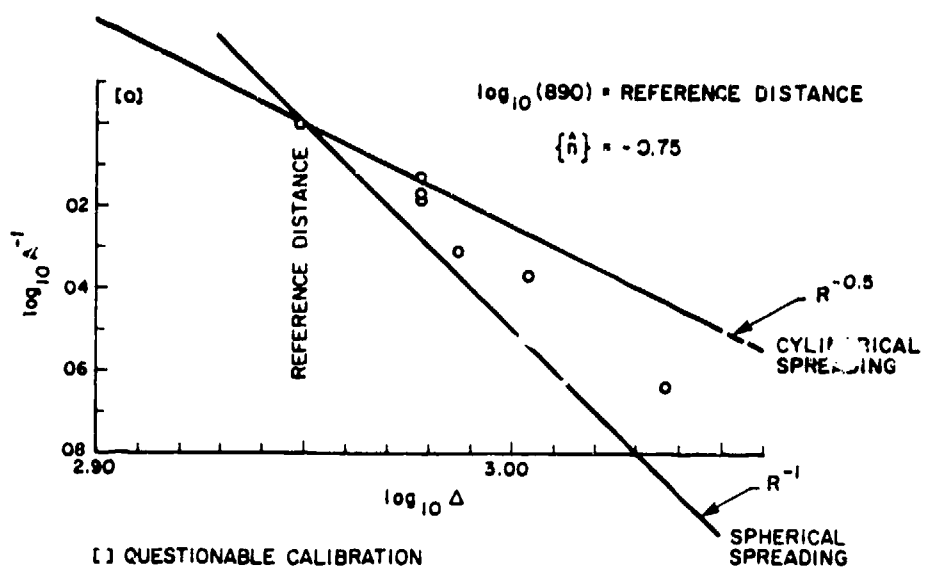


Figure 15. Optimum Attenuation Factors

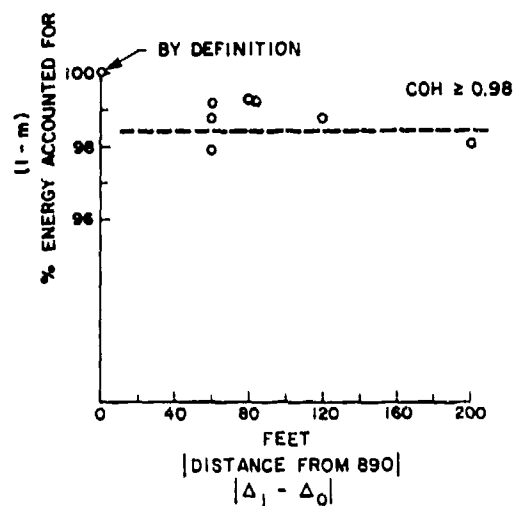


Figure 16. Bandpass RMS Surface Pressure

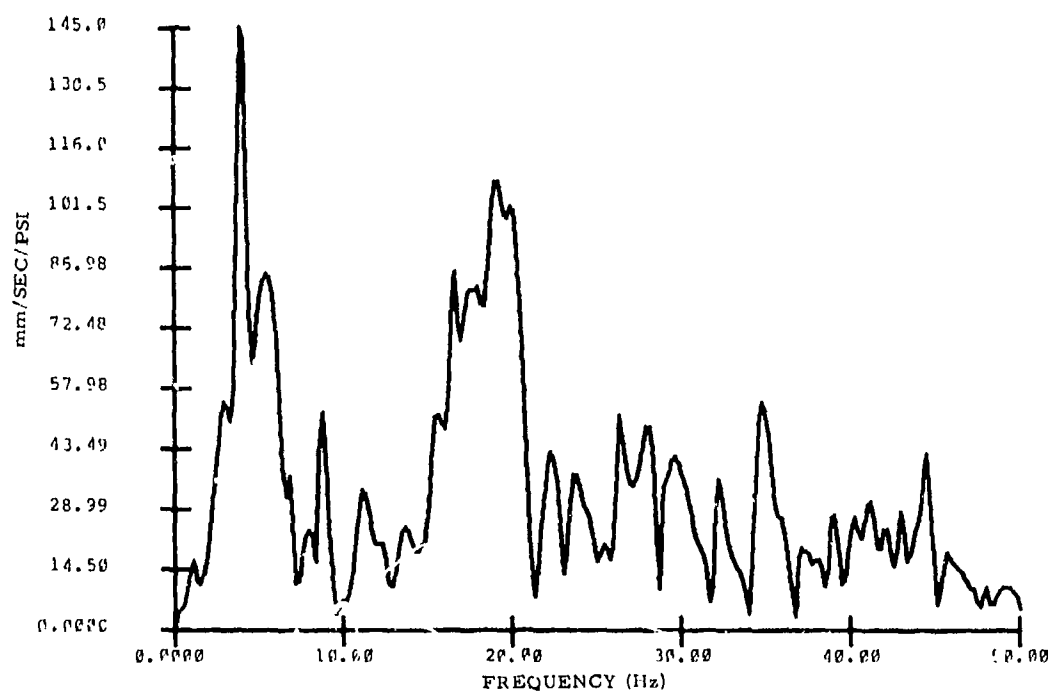


Figure 17. Observed Ground Admittance

The admittance computed here is the ratio of the FFT of the ground particle velocity and the ignition wavelet (Appendix C). As anticipated from theoretical considerations, the measured admittance is a sensitive function of frequency. Over this path at SLC-4, the fundamental air-coupled mode for acoustic loads propagating near grazing incidence ($c \approx c_\alpha$), occurs around 5 Hz. A higher mode response is also evident around 19 Hz.

4.3.2 PREDICTION

We now predict the entire ground motion sequence due to the Titan III-D launch using a linear operator that satisfies the ignition transient's admittance. Figure 18 depicts the true and predicted ground motion for the Titan III-D launch under the hypothesis that the admittance value for $c = c_\alpha$ is adequate to predict ground motion generated by the Titan at SLC-4 for the complete launch sequence. We find that the predicted motion overestimates the true during and following the time of peak loading when the rocket is at altitude.

Figure 19 shows the growth in the relative ground motion prediction error as it relates to the Titan's altitude and launch time. Ground motion estimates that are in harmony with $Y(c_\alpha, f)$ produce progressively larger relative error as the Titan III-D gains altitude, particularly above 500 ft (152 m). This finding agrees with our model response at higher phase velocities. The seismic response found here is smaller and shifted in frequency at the higher phase velocities. As in the model, we find that the seismic energy leaks out of the surficial layer. In turn, an accurate forecast of ground motion around and after peak loading requires that the admittance prediction operator $Y(c, f)$ reflect the change in the phase velocity of acoustic load produced by the rocket at altitude; the phase velocity of the acoustic load generated by the plume is an essential parameter for making ground motion forecasts. The same can also be said of elastic structures, namely that the phasing of the acoustic load is an essential parameter for making structural response estimates.²¹

4.4 Plume Emitted Acoustics

4.4.1 TIME AVERAGING

Figure 18 depicts the surface pressure over the first 30 sec of flight as measured at a station located some 890 ft (271 m) from the SLC-4E launch pad. Following the ignition pulse, the pressure level builds for about 10 sec. By this time the Titan III-D has climbed to an altitude of about 1000 ft (304.8 m), almost directly over the launch point (see Table D1 in Appendix D). At this altitude we assume that the plume is close to steady state and undeflected; hence the pressure field is insensitive to launch pad geometry.

21. NASA Report GP-1059, Revision A (1976) Environment and Test Specification Levels Ground Support Equipment for Space Shuttle Launch Complex 39:1.

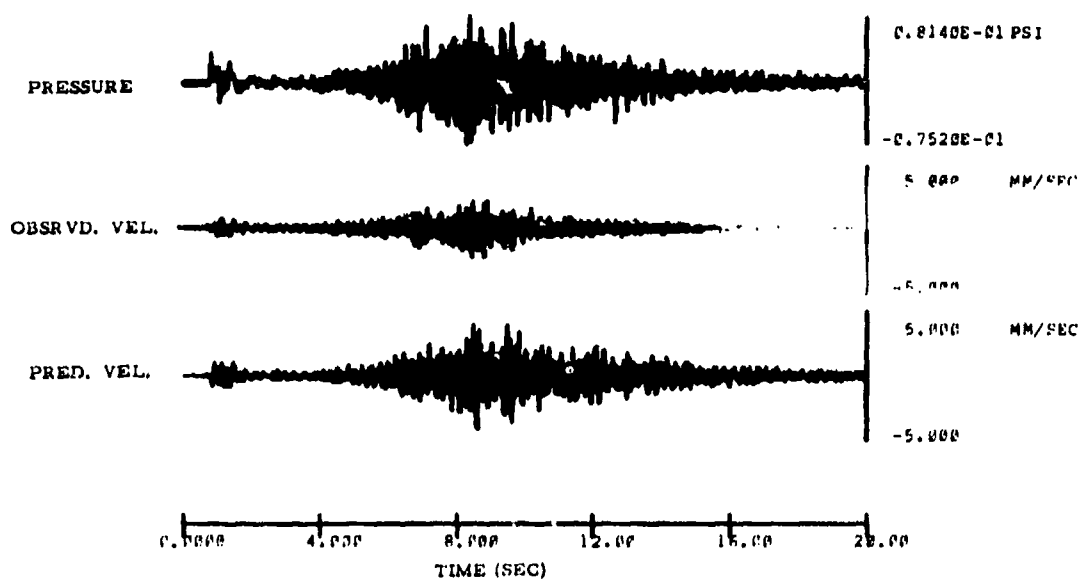


Figure 18. Predicted/Measured Ground Motions: Titan III-D

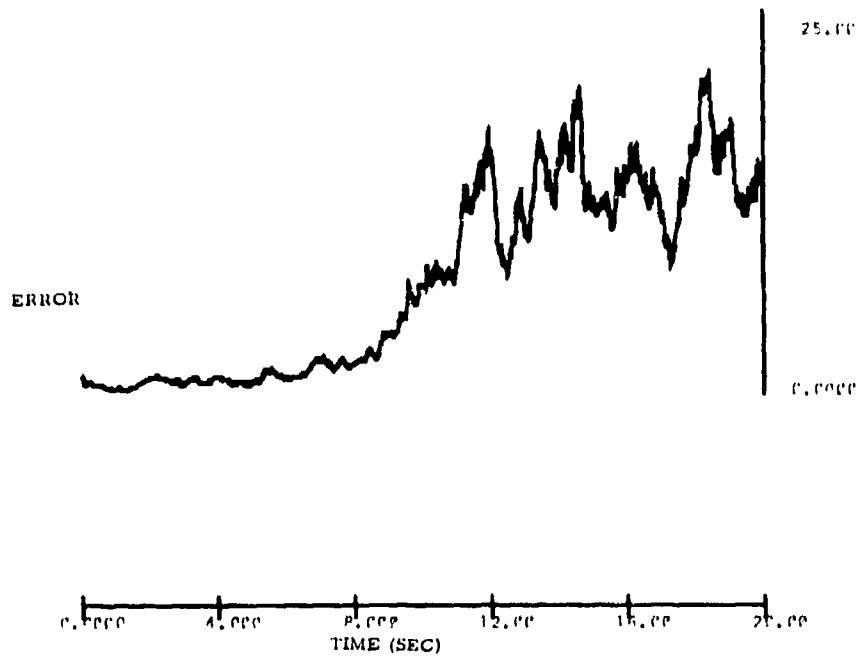


Figure 19. Relative Ground Motion Prediction Error

For a fixed observer, the surface pressure, $p_s(t)$, emitted by the plume appears as a transient, existing only in the interval $(0, T)$. In turn, all statistical time averages using $p_s(t)$, such as autoconvariance, and consequently power spectral density, are formally zero²²; that is,

$$c_{pp}(\tau) = \frac{1}{T} \int_{-T/2}^{+T/2} p_s(t)p_s(t + \tau) dt = 0 .$$

A correct estimate of the power spectral density of the pressure generated by the undeflected steady state plume requires that the temporal effects due to rocket motion be suppressed. To do this, we must locate and compensate for the motion of the plume acoustic source in the observer's coordinates.

To demonstrate the point about time averages, we compute an ensemble of root mean square pressures using the measured surface pressure and different averaging times. The resulting values are plotted in Figure 20 for a common start time. As expected, the calculated values are sensitive both to epoch and duration. Spectral estimates obtained by time averaging are affected in precisely the same manner. Discordant power spectral estimates can be expected when averaging times are not specified. Unfortunately, much of the rocket literature suffers from this elementary defect.

4.4.2 PLUME EMITTED SURFACE PRESSURE

During the early segment of flight, we represent the pressure $p_s(t)$, observed at a fixed ground station due to the undeflected steady state plume, to be the resultant of a purely path dependent function, $G(r, t; r_o, t_o)$, and a directionally sensitive source shaping operator, $P_\phi(t_o)$, that convolves with a zero mean, stationary, independent, normal process, $N(0, \sigma^2)$:

$$p_o(t) = H(t)*V_\phi(t)*G(r, t/r_o, t_o)*P_\phi(t_o)*\sigma + \epsilon(t_o) \quad (3)$$

where $\langle \epsilon(t_o) \rangle = 0$ and $\langle \epsilon(t_o)*\overline{\epsilon(t)} \rangle = 1 \cdot \delta(t)$.

As represented here, the plume is replaced by an equivalent axial-symmetric source (see Figure 21), with R the observer-source distance and ϕ the observer-source elevation angle. In turn, t is the observer's time to include the propagation delay and $V_\phi(t)$ is an operator that modifies the free field pressure to account for the atmospheric-ground structure. $H(t)$ is the impulse response of the measuring system.

22. Lee, Y. (1960) Statistical Theory of Communication, John Wiley and Sons, N.Y.

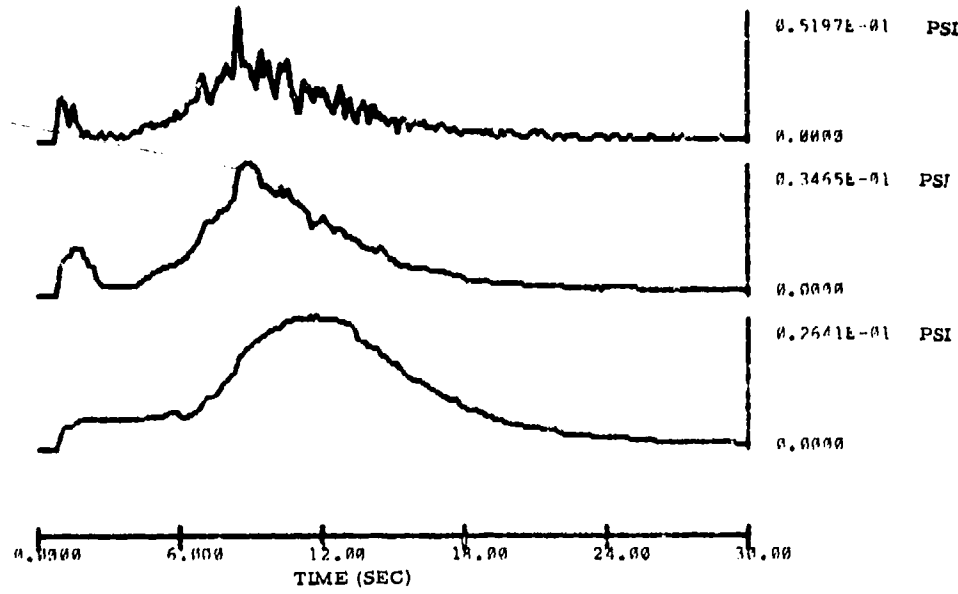


Figure 20. Broadband RMS Surface Pressure

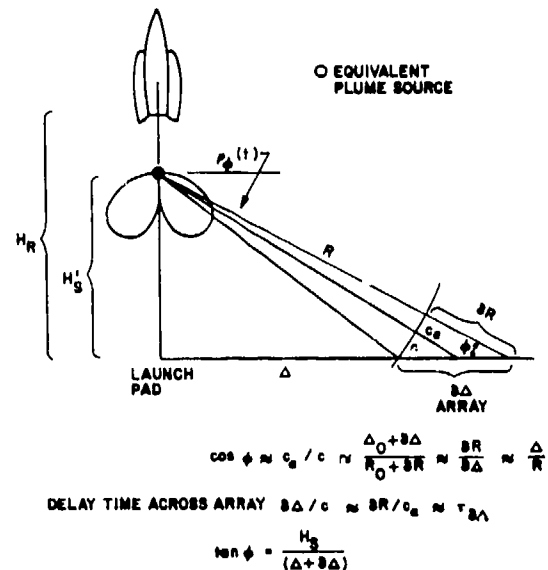


Figure 21. Rocket Source Geometry

We now represent the path dependency for the emitted acoustics in a homogeneous atmosphere as

$$G(r, t, t_0) \approx \delta \frac{[R/c_\alpha - (t - t_0)]}{R}$$

with $R, (t - t_0) > 0$.

Near the ground surface, $V_\phi(t) \approx 2$ for all but near the air-coupled frequencies. To these approximations, the measured surface pressure at an offset Δ is taken to be:

$$p(\Delta, t) \approx 2 \cdot H(t) \cdot \delta(R/c_\alpha - (t - t_0)) / R \cdot P_\phi(t_0) \cdot e(t_0) . \quad (4)$$

For a vertical launch, the surface pressure is

$$P_\Delta(t + \Delta c/c_\alpha^2) \approx 2/\Delta(c/c_\alpha) \cdot P_\phi(t) \cdot e(t) \quad (5)$$

where the delay time, $\Delta c/c_\alpha^2$, and gain factor, $2/\Delta(c/c_\alpha)$, are time dependent because $c = c(t)$.

In turn, pressure amplitude ratios across our array are

$$|P_\Delta/P_{\Delta_j}| = 1 - (c_\alpha/c)^2 \cdot \delta_{\Delta_j}/(\Delta + \delta_{\Delta_j}) \quad (6)$$

with the delay times

$$\delta_{\Delta_j}/c . \quad (7)$$

Much as before we test our representation of surface pressure through an ensemble of "best" amplitude and delay pairs by fitting our observations in a least squares sense to the form of Eqs. (6) and (7). The best amplitude ratios (Figure 22), and delay times (Figure 23), are obtained for a 2.56-sec data time gate during peak surface loading. The amplitude ratios and delay times so obtained are consistent with an "equivalent" plume source at an elevation of 350 ft. (107 m), well below the Titan rocket.

We again evaluate our representation by computing the relative error between the predicted and observed pressure values with separation, as seen in Figure 24. The error now is a sensitive function of separation. Indeed, for a separation of 250 ft. (76.2 m), the mean square error is about 50 percent of the observed value.

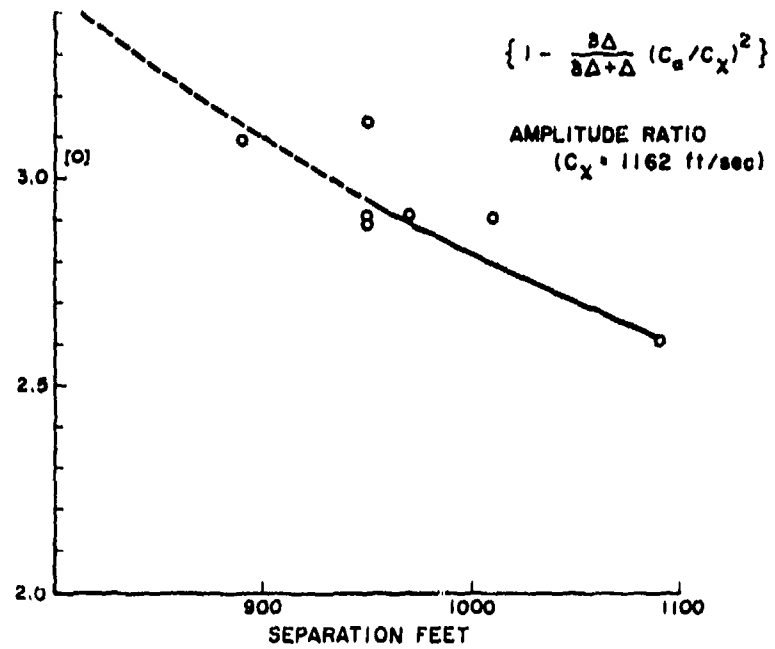


Figure 22. Amplitude Ratio During Peak Loading

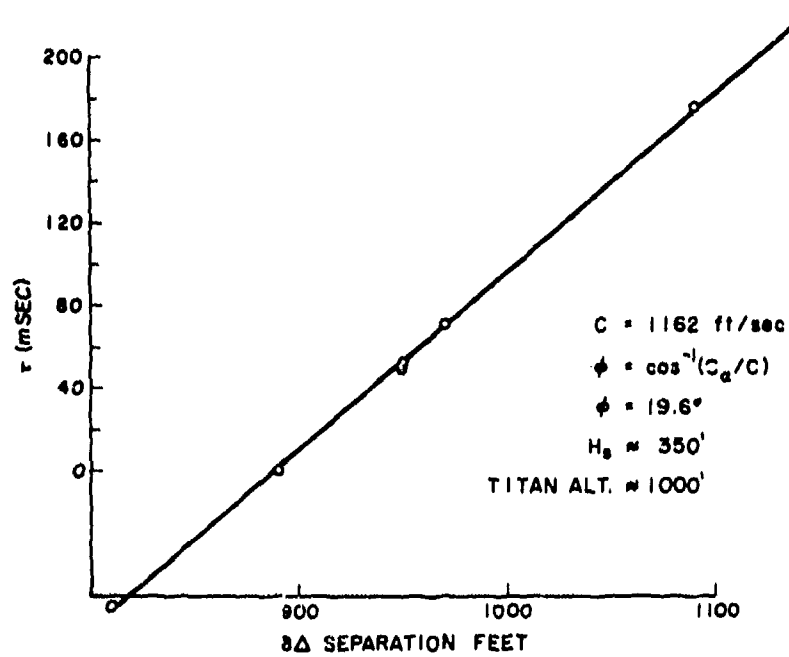


Figure 23. Phase Velocity During Peak Loading

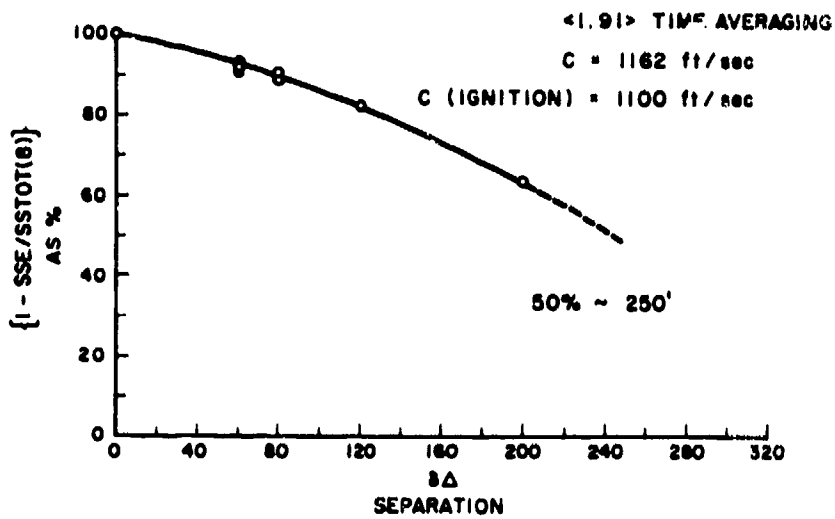


Figure 24. Residual Error for Maximum Loading

By ignoring the motion of the rocket over the sample time gate, we misrepresent the actual phase change in the acoustic load. The best average phase shift underestimates the true shift at the beginning of the sample. Towards the end of the sample, the best average value is too large.

4.4.3 PHASE VELOCITY

In order to sqrt out plume and propagation properties, we make a succession of phase velocity estimates for the plume generated pressure propagating over our array. Figure 25 is a set of median phase velocities calculated from the phase shifts of a sequence of overlapping 2.56-sec samples (Appendix E).

We now set out to show that the propagation is nondispersive; that is, that the phase velocity is independent of frequency. As computed from the cross spectra, "phase velocity" is a set of magnitudes ordered by frequency (see Figure 26). We now treat the calculated velocities to be inconsistent independent estimates about a constant velocity. Under this assumption, we can expect that the mean number of runs computed from sign changes in the first differences in our phase velocity estimates is $[(2n - 1)/3]$ where n is the total number of estimates.²³ For large n the number of runs tends to be normally distributed about the median with a standard distribution of $[(16n - 29)/90]^{1/2}$. For our tests $n = 127$, hence the expected number of runs is 84 with a standard deviation of 5. For nondispersive propagation

23. Owen, D. (1962) Handbook of Statistical Tables, Addison-Wesley Publishing Co., Reading, MA.

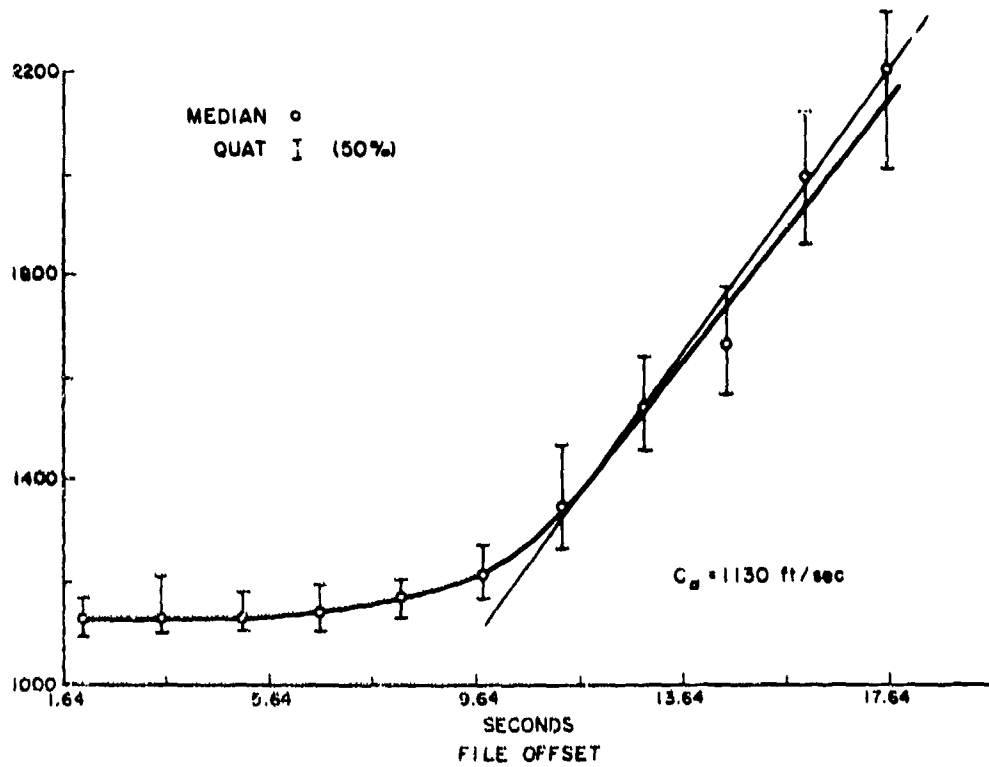


Figure 25. Estimated Phase Velocity vs. Time

we can expect that for about 70 percent of our trials the number of runs will lie in the range $79 \leq R\# \leq 89$. Figure 27 gives the actual number of runs obtained for the launch as they relate to sample start time. We conclude that acoustic phase velocity over the array is independent of frequency. Plume generated propagation delays can be calculated simply from $(R/c_a) = \tau$. Also, the "equivalent" plume source height is independent of frequency. Our calculations do not support the notion that the "source pressure" is refracted through an angle proportional to wavelength.

4.4.4 COHERENCE

An estimate of coherency based on observations taken over the entire launch sequence is calculated after the manner of Hinich and Clay¹⁵ for a station pair located 200 ft. (61 m) apart (Figure 28). This ordinary estimate of coherency leads to an "incoherent pressure field" for all but the lowest frequencies. The low coherency values found here in our primary measurement band (3-30 Hz) reflect the nonstationarity of the amplitude and phase relation of the surface pressure during launch. To show that this is indeed the case, we now calculate the

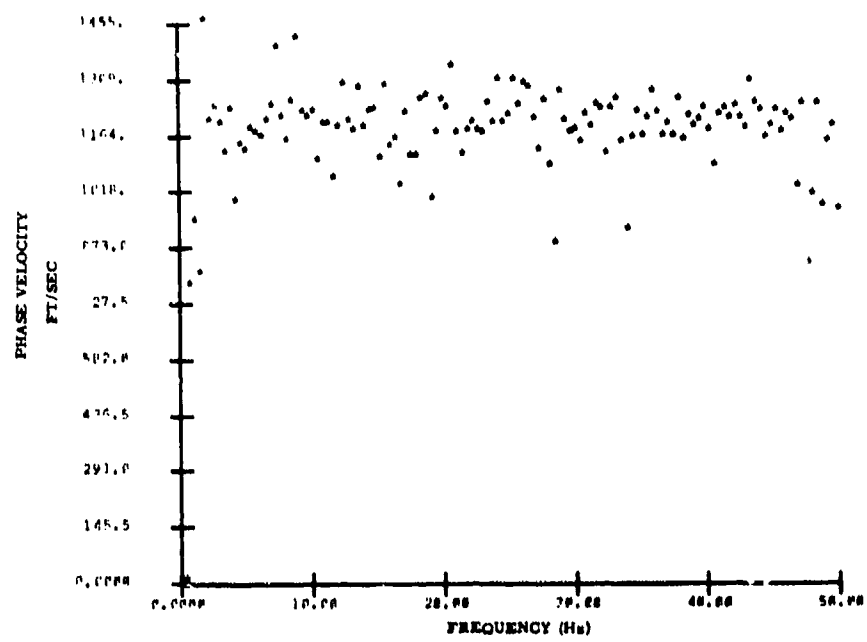


Figure 26. Phase Velocity: 8.7 sec After Launch

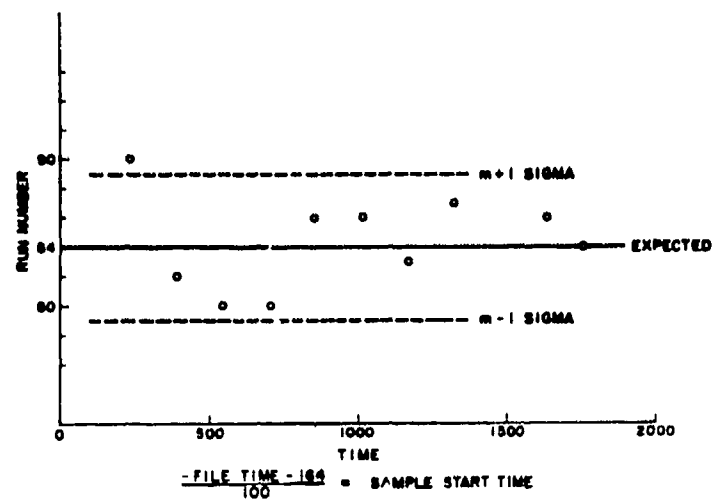


Figure 27. Runs Test for Dispersion

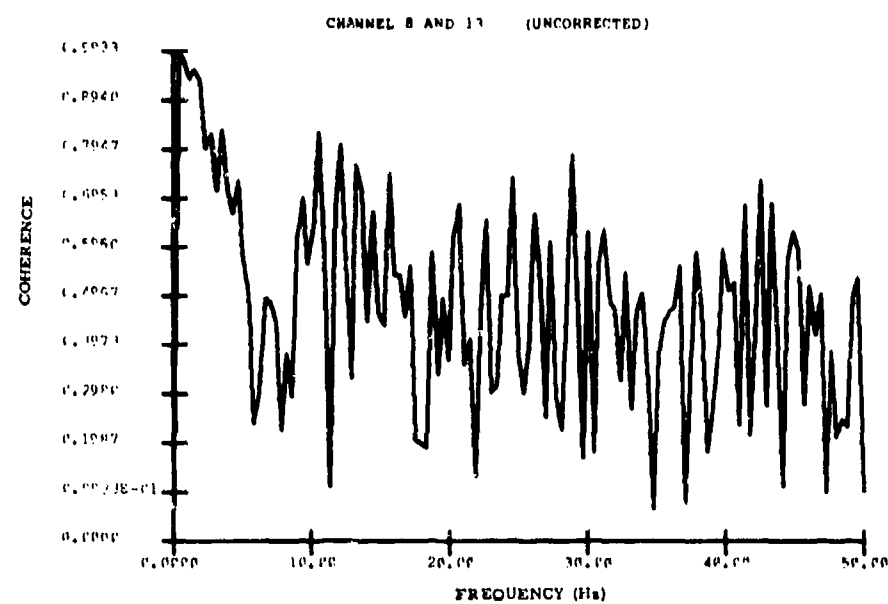


Figure 28. Coherency Estimate

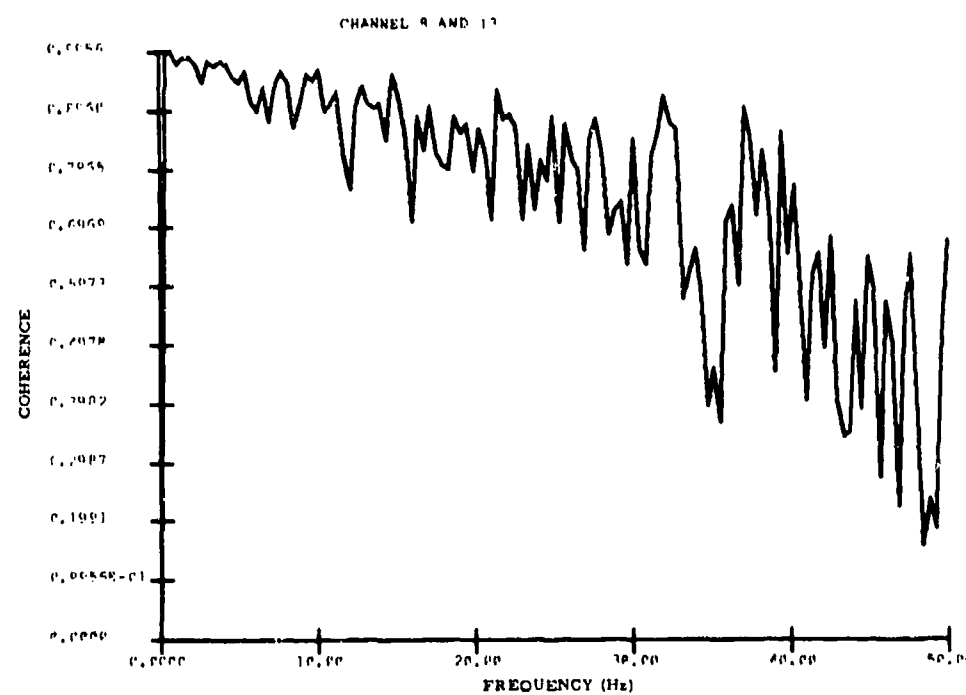


Figure 29. Spacial Coherence

"spacial coherency" of the surface pressure for the same station pair by compensating our pressure phase measurements in accordance with our estimate of $c(t)$ and the relations of Eq. (6) and (7). Figure 29 is our estimate of coherency after the pressure measurements are weighted and shifted to agree with our estimate of $c(t)$. The pressure field is now quite coherent up to 30-35 Hz. A stationary amplitude and phase relation results between field points in our primary passband when the data are corrected for rocket climb-out.

The loss of coherency above 35 Hz in Figure 29 is readily accounted for by the ambient noise measurement and the low protection ratio for the digitized data much above 35 Hz. As can be seen in Figure 30, the upper limb of the plume generated acoustic load falls into the ambient noise shortly after the time of peak loading.

In our passband we find that the plume generated acoustic load is spacially coherent for stations separated by as much as 200 ft. (61 m).

4.4.5 SPECTRAL ESTIMATES

Stable, high degree of freedom (DOF) plume spectral estimates at some elevation angle ϕ can be obtained in a number of ways. One obvious technique is to increase the DOF and thus acquire stability by averaging spectra over a number of launches; that is, ensemble average. In turn, for any one launch an estimate can be stabilized by averaging over an ensemble of measurements. Figure 31 is our spectral estimate during peak load obtained by averaging periodograms over eight stations.

Lastly, we can increase DOF by averaging over frequency. Here we attempt to construct high DOF spectra by fitting periodograms to a spectral form over our entire measurement passband. Both from physical considerations²⁴ and a number of experimental studies,¹⁹ the power spectral density of the surface pressure disturbance emitted by an undeflected chemical rocket plume is found to closely follow the form

$$P_{pp}(\omega) = 4P_0/\pi\omega_m(\omega/\omega_m + \omega_m/\omega)^{-2} \quad (8)$$

with $P_0/\pi\omega_m$ the value at the spectral maximum, ω_m the angular frequency at the spectral maximum, and P_0A the overall sound power.

We now test the hypothesis that the acoustic power spectra density emitted by the steady-state undeflected Titan III-D plume can be cast in the form equivalent to Eq. (8). The pressure measured at a surface station 950 ft. (290 m) from the

24. Powell, A. (1964) Theory of vortex sound, J. Acoust. Soc. Am. 36:177-195.

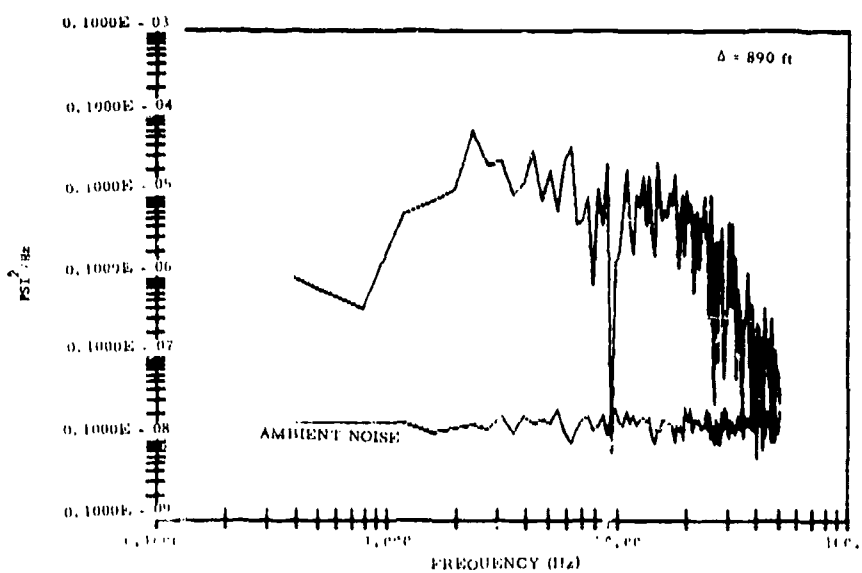


Figure 30. Observed Spectra

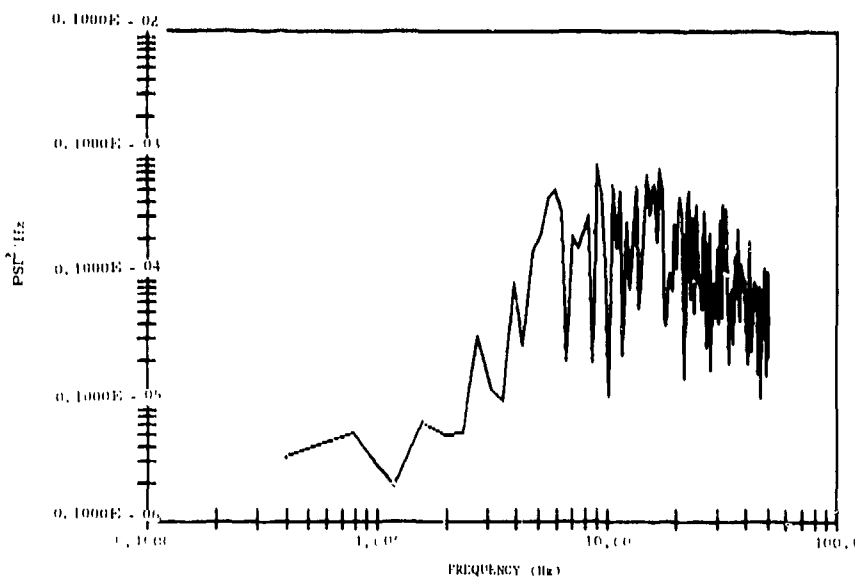


Figure 31. Peak Load Spectral Estimates

launch pad is used to generate a succession of two DOF periodogram estimates based on measurements taken in 2.56-sec sample gates. The spectral estimates calculated here are unbiased, inconsistent estimates of a stationary stochastic process when the time samples are concatenated with a like number of zeros before transforming.²⁵ The spectra constructed here are power spectra in the sense that they satisfy Parseval's relation in the time interval of the sample, namely

$$\langle p^2 \rangle_T = \int_0^{f_n} P_{pp}(f) df = m_o$$

where $T = 2.56$ sec and f_n is the Nyquist frequency.

The spectral form of Eq. (8) is fitted to each periodogram to obtain a best estimate of (P_{0A}, f_m) in the sense that the mean square difference between the two representations is minimized by our choice of P_{0A}, f_m . Figure 32 shows the best spectra calculated around the time of maximum acoustic loading, superimposed on the calculated periodogram points.

We now construct a table of (P_{0A}, f_m) values over a sequence of overlapping 2.56 sec gated samples (see Table 1). Also included in Table 1 is the overall mean square surface pressure estimate developed by the model rocket plume. It is worth noting here that the theoretical total pressure level is less than the measured value for sample midtimes after 15 sec. At such times the acoustics are abating while the turbulence at the site is well developed.

A number of tests were conducted to evaluate the hypothesis that the measured spectra did not depart significantly from the form of Eq. (8). One such test result is given in Figure 33. The figure is a probability paper plot of the distribution of the observed residuals against the residual distribution expected for a χ^2_2 variate with two DOF: the expected distribution, had we fitted the periodogram ordinates to the true spectra. The paper is constructed so that the acceptance criteria is one of simply accepting the plotted values to lie on the indicated straight line. Both from such tests and tests based on an acceptance range in our Figure of Merit obtained from simulation,²⁶ we conclude that the periodograms are well represented by an equation of the form of Eq. (8) particularly around the time of maximum acoustic loading.

-
- 25. Ywen, C. (1979) On the smooth periodogram method for spectrum estimation, Signal Processing 1:83-86.
 - 26. Hartnett, E., and Carleen, E. (1980) Characterization of Titan III-D Acoustic Pressure Spectra by Least Squares Fit to Theoretical Model, AFGL-TR-80-004, AD

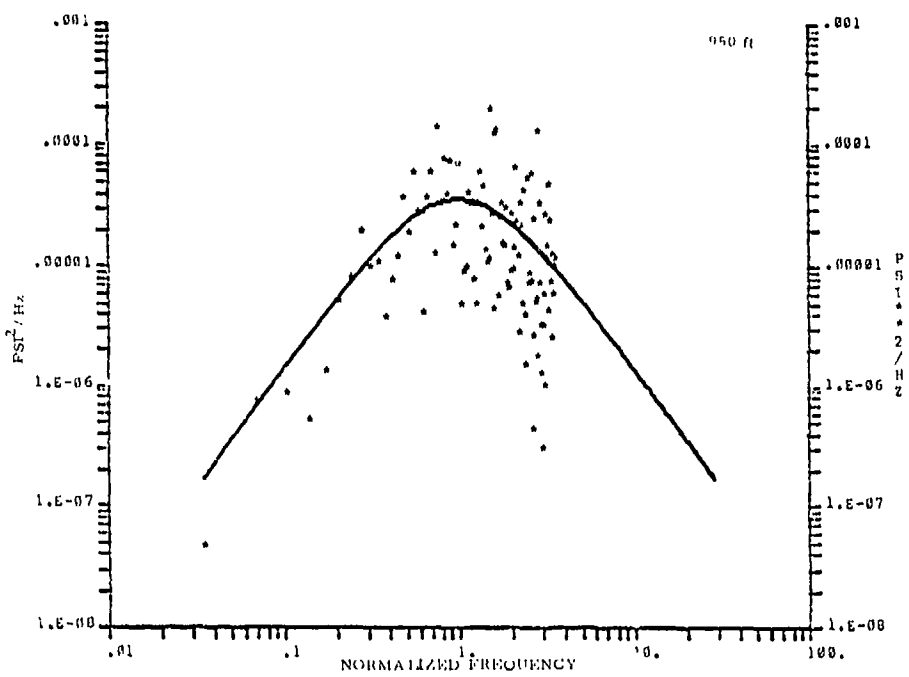


Figure 32. Spectral Estimates: 8.51 sec After Ignition

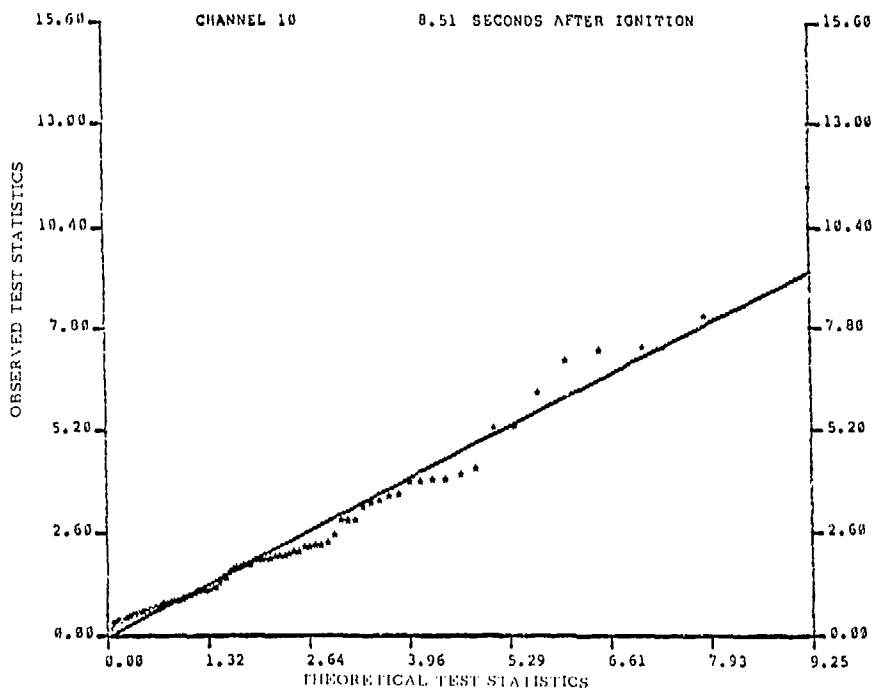


Figure 33. Theoretical Test Statistics Acceptance Test

Table 1. Overall Sound Power Values

Start Time After Ignition (sec)	f_o (Hz)	Theoretical P_o (psi^2) db	Error $E\left(\frac{(\text{psi}^2)^2}{\text{Hz}}\right)$	Observed Power (psi^2) $0 < f < 50 \text{ Hz}$	Spectral Maximum $\frac{\text{psi}^2}{\text{Hz}}$	Figure of Merit
3.83	6.798	$8.477(10^{-5})$ 130.0	$4.022(10^{-10})$	$7.931(10^{-5})$	—	214.6
5.39	14.269	$6.741(10^{-4})$ 139.0	$1.268(10^{-8})$	$3.875(10^{-5})$	$1.5006(10^{-5})$	1.005
6.95	12.071	$1.608(10^{-3})$ 142.8	$5.342(10^{-8})$	$1.007(10^{-3})$	$4.2350(10^{-5})$	0.6204
8.51	11.190	$1.257(10^{-3})$ 141.7	$6.848(10^{-8})$	$8.264(10^{-4})$	$3.576(10^{-5})$	1.381
10.07	7.548	$6.331(10^{-4})$ 138.8	$1.648(10^{-8})$	$4.993(10^{-4})$	$2.683(10^{-5})$	1.528
11.63	5.236	$2.845(10^{-4})$ 135.3	$5.418(10^{-9})$	$2.572(10^{-4})$	$1.730(10^{-5})$	1.813
13.19	6.097	$1.115(10^{-4})$ 131.2	$7.147(10^{-10})$	$1.035(10^{-4})$	$5.821(10^{-6})$	1.405
14.75	4.390	$4.608(10^{-5})$ 127.4	$2.198(10^{-10})$	$4.872(10^{-5})$	$3.341(10^{-6})$	2.59
16.31	2.855	$1.860(10^{-5})$ 123.4	$0.203(10^{-11})$	$2.420(10^{-6})$	$2.074(10^{-6})$	1.032

We now plot P_{OA} as it relates to the start time of the sample following rocket ignition in Figure 34. The time for a maximum P_{OA} for an observer located 950 ft (290 m) from the launch pad is about 8 sec. Following this maximum, the overall sound power estimate decays exponentially at a rate of about 2.5 db/sec.

In Figure 35, f_m is plotted as it relates to the sample start time. Over the period of estimation, the frequency of the spectral maximum decreases roughly linearly with time. The one sigma spread in f_m , found by simulation, is indicated. The shift in f_m is significant. The plume emits significantly lower frequency spectra at the higher elevation angles. The shift is well in excess of the frequency shift ascribable to the source velocity.

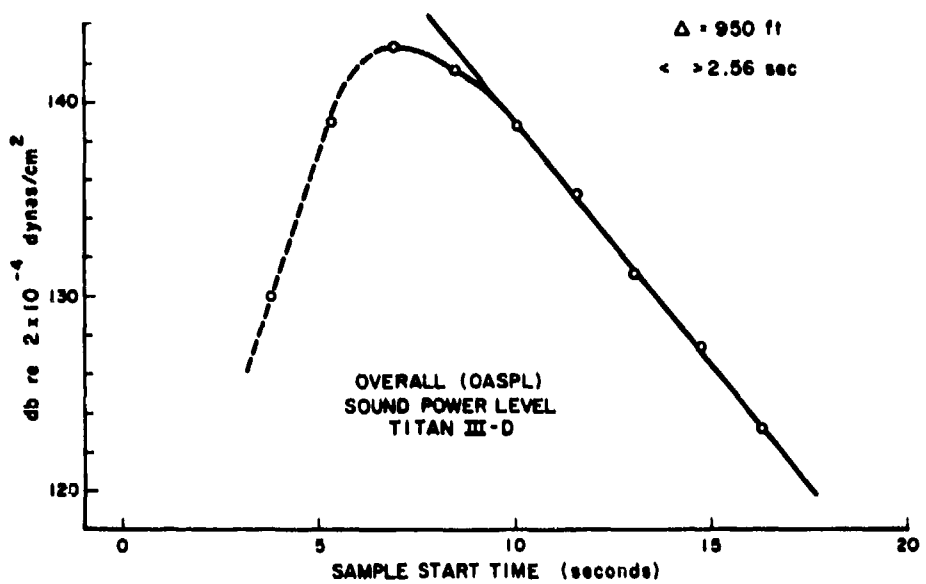


Figure 34. Overall Sound Power Level

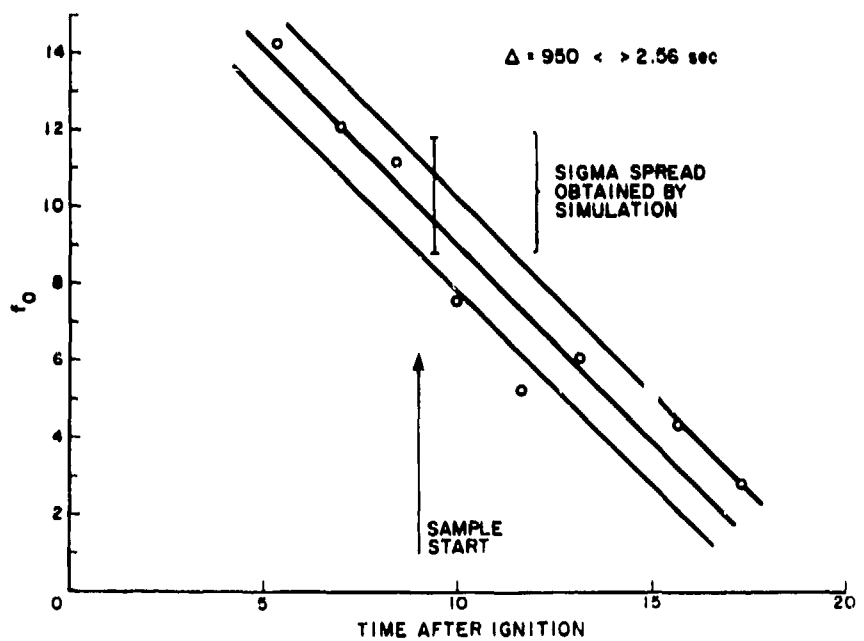


Figure 35. Frequency at the Spectral Maximum

5. ADMITTANCE ESTIMATES

Over the first 20 sec of launch, admittance estimates, based on averaging three consecutive 0.64-sec co-located pressure and ground samples, are computed. The computation is repeated every 1.56 sec following the arrival of the ignition pulse. As in the theoretical case, we again locate admittance maxima in terms of phase velocity and frequency. We find that the response maxima migrate in the (c, f) plane in the expected manner in that the "frequency" of the air-coupled disturbance decreases with an increase in phase velocity for both the fundamental and the first higher mode response, shown in Figure 36. In turn, the absolute value of the ground response maxima are given as they relate to phase velocity in Figure 37. The measured responses are substantially less at the higher phase velocities, as expected.

We now calculate the usual plume directivity value¹⁹ based on our measured overall plume pressure levels, P_{0A} , and $1/R$ attenuation for a source located near the base of the Titan (see Figure 38). If we now compare this pattern to the radiation pattern obtained using Eq. (5), an elevation angle obtained from our estimate of phase velocity, we find the usual directivity calculation poorly represents the pressure load for facility response computations (Figure 39).

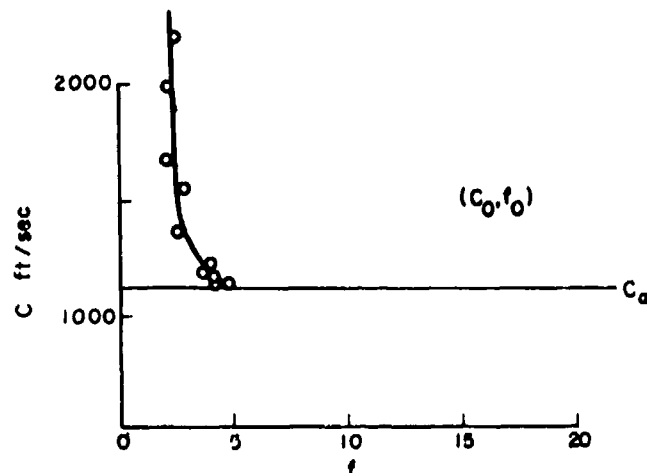


Figure 36a. Measured Admittance: Fundamental

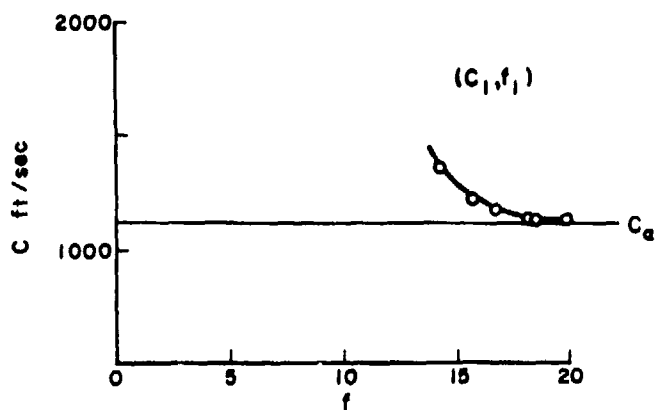


Figure 36b. Measured Admittance: First Mode

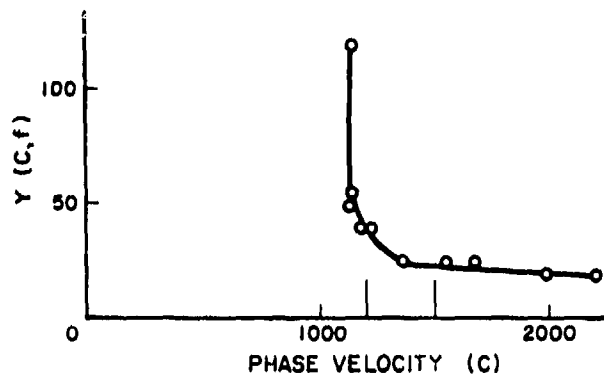


Figure 37a. Admittance Maxima: Fundamental

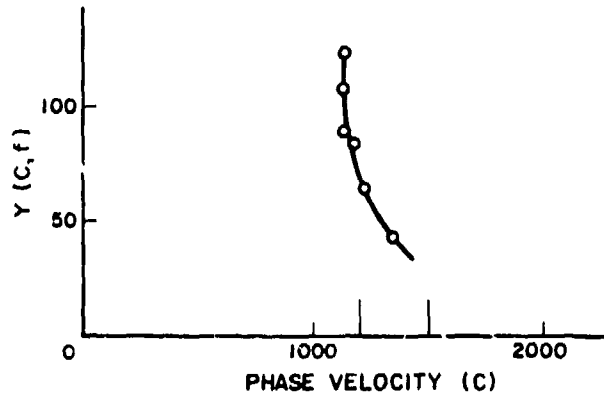


Figure 37b. Admittance Maxima: First Mode

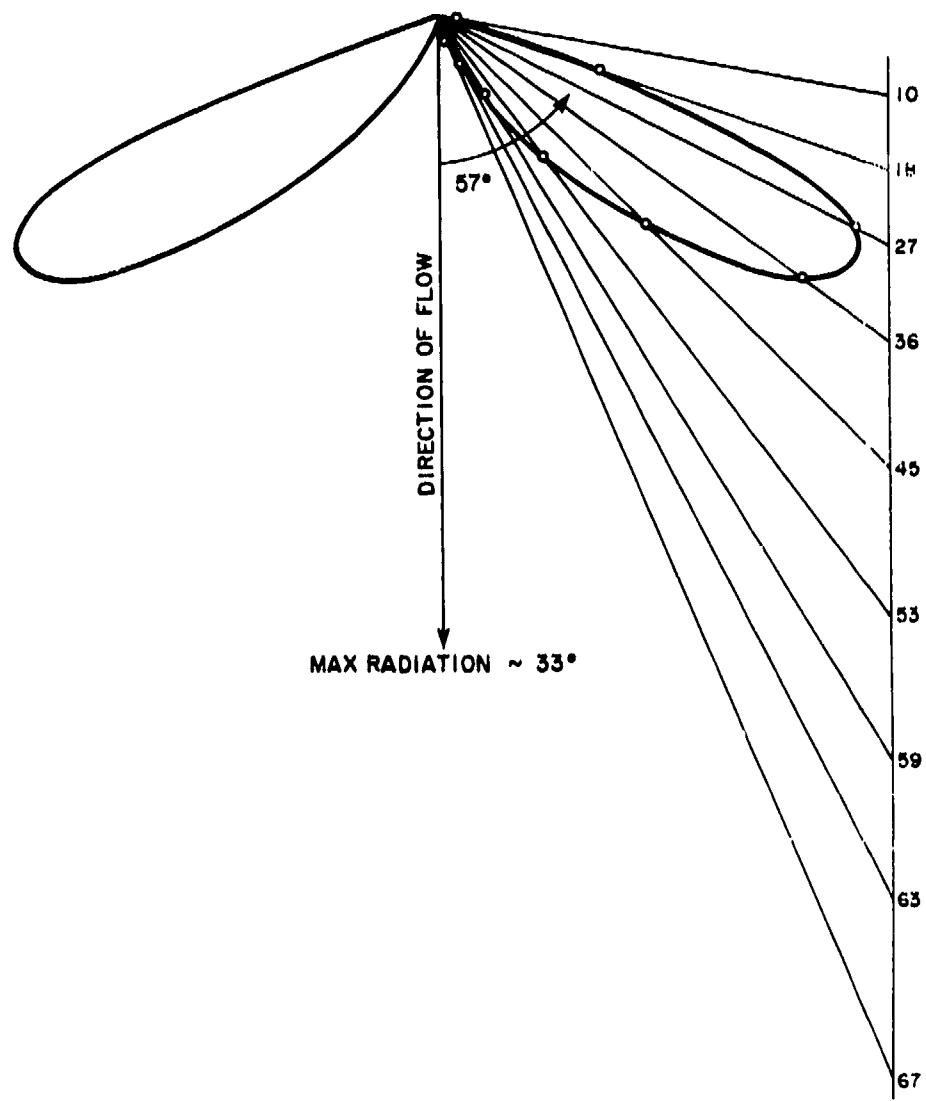


Figure 38. Apparent Directivity

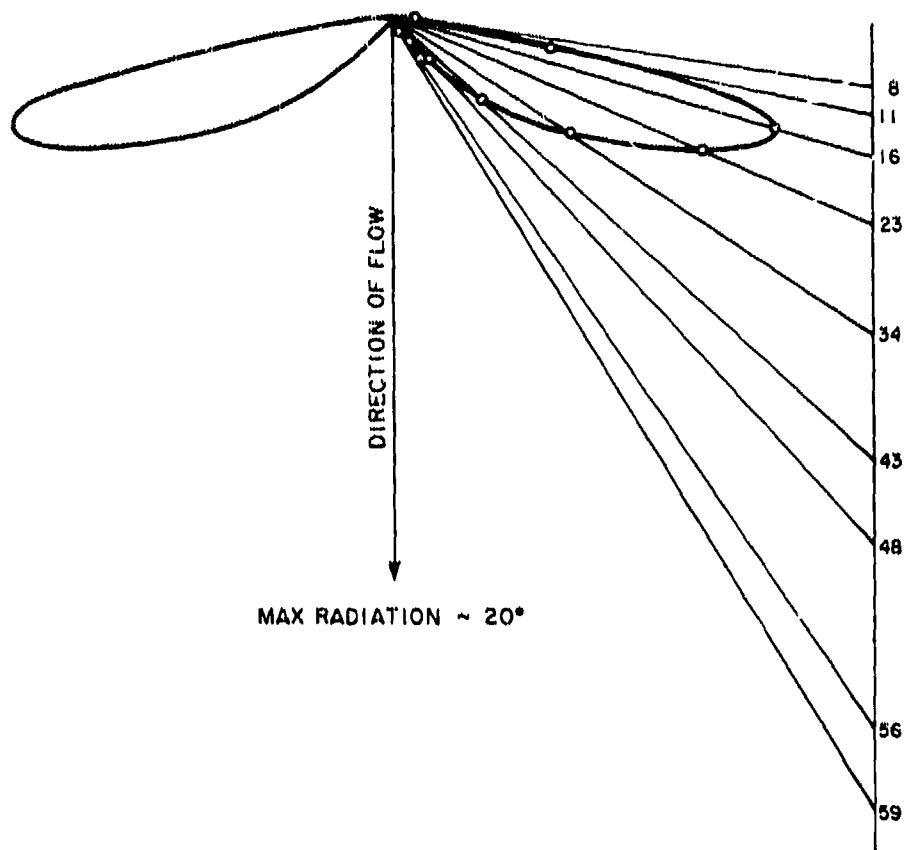


Figure 39. Radiation Pattern From Phase Velocity

6. SCALING TITAN III-D INTO STS

6.1 Power Spectra Density Estimates

The overall acoustic efficiency of undeflected chemical rocket plumes is relatively constant over a wide range of thrust levels for similar nozzle flow parameters. Table 2 summarizes the engine parameters needed to scale the acoustic loads due to Titan III-D into STS launches.^{21, 27} We now normalize our estimate of the Titan III-D spectra observed at 950 ft. (290 m) around peak loading using the scaling parameters given in Table 2. In standard form, shown in Figure 40, the maximum spectral value is expected at $f(de/U_e) = 0.02$; our measured value is 0.0198. In standard form we expect the spectral maximum $W(f)/WOA \cdot (U_e/de)$ to be 10 db in excess of the overall power. Our measured value is 12 db. Our

^{27.} Smith, J., The Aerospace Corporation, Ltr dated 4 January 1980, Rocket Engine Parameters.

Table 2. Rocket Engine Parameters

Number of Engines	Nozzle Exit Diameter (de) in. (cm)	Exhaust Velocity at Sea Level (U_e) ft/sec (m/sec)	Total Power at Liftoff lb ft/sec (kg m/sec)	STROUHAL#
SRB 2	141.7(359.9)	6440(1963)	$3.317^{10}(4.596^9)$	-
SSME 3	92.0(234)	9730(2966)	$1.218^{10}(1.687^9)$	-
STS -	-	-	$4.535^{10}(6.283^9)$	0.00293f
TITAN-D 2	106.6(270.8)	7676(2340)	$1.921^{10}(2.661^9)$	0.001637f

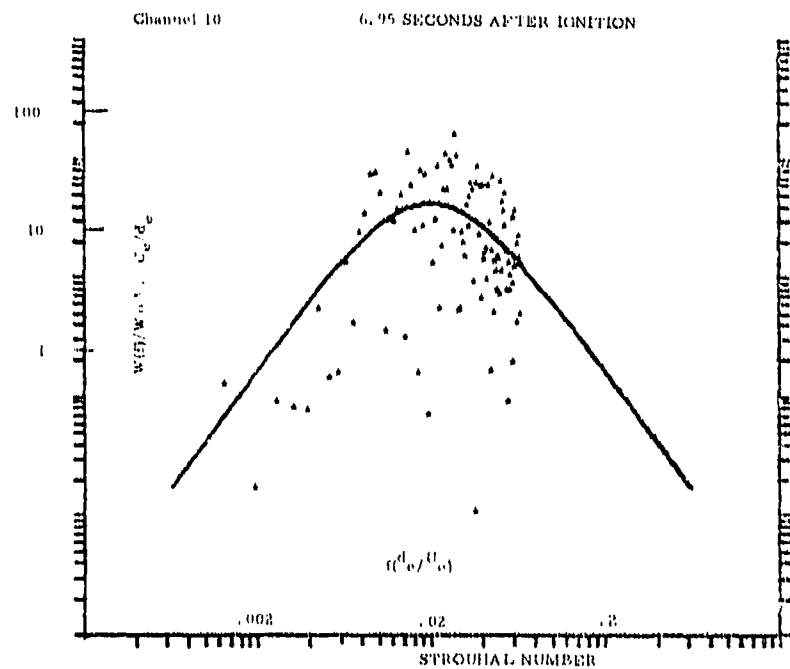


Figure 40. Titan Spectra in Standard Form

spectra for a Titan III-D satisfies the standard form spectra for undeflected chemical rocket plumes in the thrust range 350 to 7,000,000 lb (159 to 3,180,000 kg).²⁰

We now construct a normal stationary time series that fits the spectral properties of the surface pressure expected at a point 950 ft (290 m) from the pad for a STS launch around the time of maximum loading. The design OASPL for the STS Simulation is 2.36 times that of the Titan III-D; that is, 2.36 is the ratio of the total power levels between the two systems at launch. In Figure 41 we compare the spectra for the two systems. Each spectra satisfies the standard form spectra shown in Figure 40, when the scaling values of Table 2 are applied. We find that for structural responses above 20 Hz the expected motion levels due to STS and Titan launches differ only by a few db. For low mode ground and large structure responses, the expected motion environments of the two systems differ significantly; that is, < 20 Hz.

In order to address the problem of repeated launches we construct STS spectrum estimates at the 50 and 97.5 percent confidence levels by appealing to the ergodic hypothesis and the χ^2 distribution of our test statistics.²⁶

$$\chi^2(x) = F(2P_j^l / P(l_j)) \quad \text{DOF} = 2$$

For example, the lower bound spectra $P_{50}(f_j)$ shown in Figure 42 will be exceeded 50 percent of the time, on the average, by a periodogram estimate at the frequency, f_j , when ensemble averages equal time averages.

6.2 OBSPL Estimates

We now compare our forecast, based on scaling up power spectra obtained from one Titan launch around the time of maximum acoustic loading, with OBSPL estimates obtained by scaling down ensemble averages of Saturn V launches during the liftoff peak.²¹ In order to compare the two "spectra," a number of adjustments must be introduced. The factors needed to convert our results into OBSPL for different confidence levels are given in Table 3.

The table $\gamma_{N\%}$ quantities given here are needed to adjust the χ^2 distributions of the OBSPL estimates when integrating constant resolution spectra; that is,

$$\text{DOF} - \gamma_{N\%} = \frac{1}{2\text{DOF}/2 \cdot \sqrt{\text{DOF}/2}} \cdot \int_0^{\gamma_{N\%}} x^{(\text{DOF}-2)/2} \cdot e^{-x/2} dx = N\% / 100$$

where $N\% = 50, 97.5$.

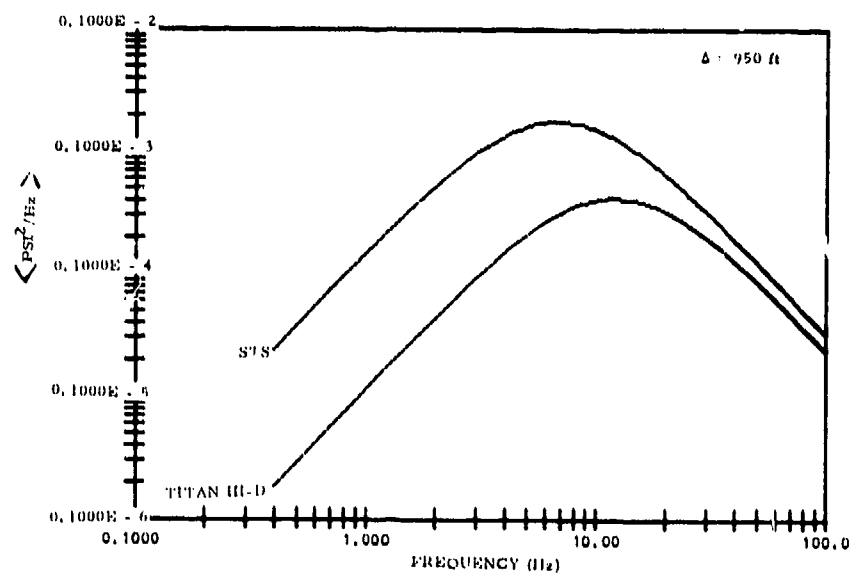


Figure 41. Acoustic Surface Pressure Around Maxima Loading

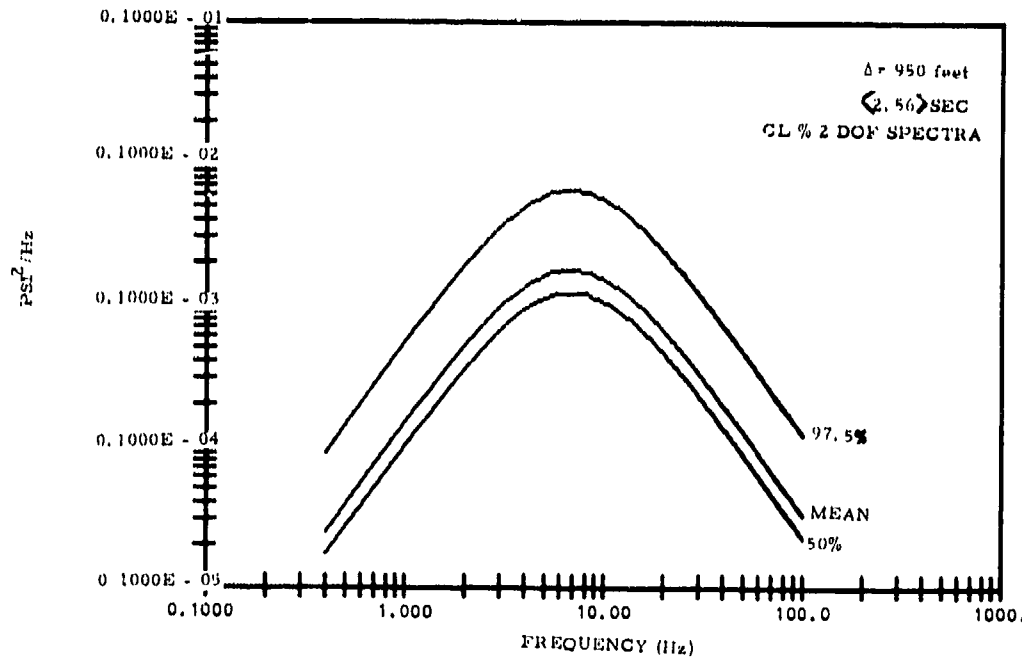


Figure 42. STS Surface Spectra

Table 3. Overall Sound Pressure Levels

f_c	$E\{\text{OBSPL}\}(2.56)$	DOF	$\gamma_{50\%}$	$\gamma_{97.5\%}$
2	129.4	6	0.892	2.408
4	137.2	12	0.942	1.945
8	141.3	26	0.973	1.612
16	141.7	54	0.987	1.411
315	140.2	106	0.993	1.287
63.0	137.5	214	0.997	1.189

Figure 43 summarizes our STS OBSPL forecast for surface pressure at the 50 percent and 97.5 percent confidence levels. In the usual fashion, the dispersion about the expected value is sensitive to the DOF of the estimate. For an averaging time as large as 2.56 sec, the expected and median spectral estimates differ by less than 5 percent above 8 Hz. For bandwidths somewhat larger than 30 Hz, there is, on the average, only a 1 db difference between the 50 and 97.5 percentiles for the two distributions.

We now must allow for differences in our OBSPL due to differences in averaging times. In Figure 44 we plot the maximum of the RMS pressure level found over passband for the Titan launch as it relates to averaging time. For the Titan, we have a 3.3 db separation between the RMS pressure computed for a 0.3 sec averaging time and one based on 2.56 sec. For large DOF estimates (greater than 25) we now simply add 3.3 db to our results given in Figure 43 to compensate for time averaging "on the order of 0.3 sec" over a lift off peak that lasts for 2.3 sec (based on 3 db points of the SATURN V OASPL envelope).²¹ Our results now are quite close to the NASA mean OBSPL curve for STS obtained by down scaling SATURN V data. All our results, seen in Figure 45, are well below the NASA 97.7 percent confidence level forecast. Indeed, the constant 3.1 db separation between the 50 and 97.7 percent confidence level appearing here cannot be explained in terms of the equivalence of ensemble and time averages.

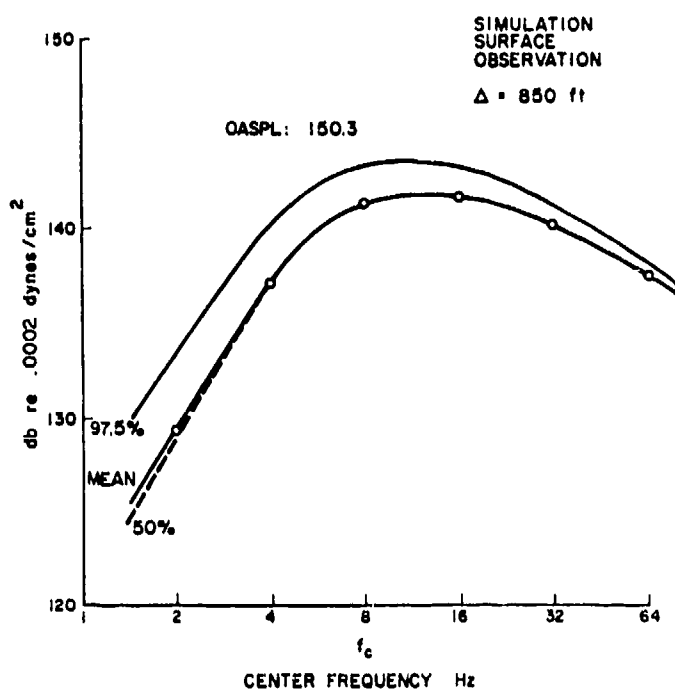


Figure 43. STS OBSPL Estimates: $\langle \rangle$ 2.56 sec

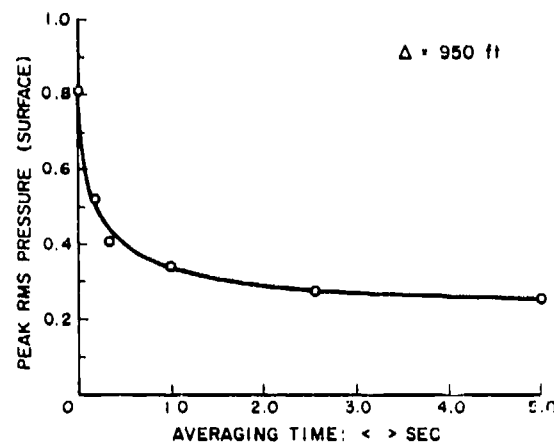


Figure 44. Effect of Averaging Time

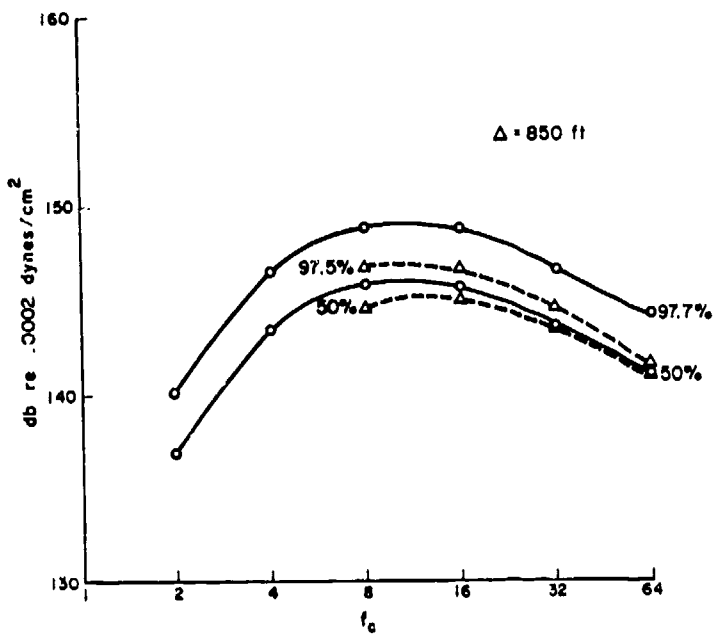


Figure 45. STS Estimates OBSPL: $\langle \cdot \rangle = 0.3 \text{ sec}$

7. GROUND RESPONSE AT SLC-6

The ground response in the vicinity of the Launch Control Center (LCC) at SLC-6 was measured for an acoustic source located 300 ft (91.4 m) above the STS launch pad, as shown in Figure 46. The ground admittance measured over this path is dominated by the fundamental air-coupled wave. The frequency of the air-coupled term found near the LCC is at 6 Hz. This frequency is significantly higher than the frequency for the fundamental air-coupled wave excited at SLC-4. The ready explanation for the difference lies in a difference in the thickness of the unconsolidated sediments at the two sites.

We now construct a sample STS pressure $P(t)$ to simulate the expected maximum loading for an elevated plume source for the distance to the LCC; that is,

$$p(\Delta_{\text{LCC}}, t) = 2/\Delta_{\text{LCC}}(c/c_\alpha) \cdot P_\phi(t) * \Sigma(t)$$

where as before $\Sigma(t)$ is from a $N(0, \sigma)$, stationary process and $\langle P_\phi * \bar{P}_\phi \rangle$ satisfies the standard form spectral figure given in Figure 41 for the STS at altitude.

The sample pressure in turn is passed through an operator that satisfies the measured, path sensitive admittance to give

$$V_{\Delta_{\text{LCC}}}(t) = Y_{\Delta_{\text{LCC}}}(t) * P_{\Delta_{\text{LCC}}}(t)$$

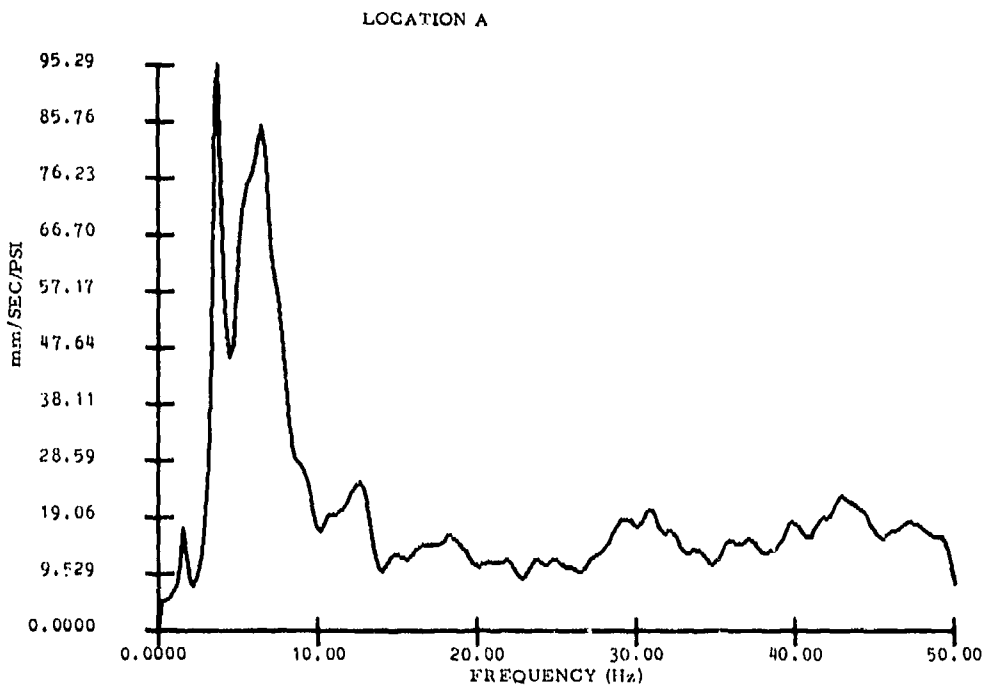


Figure 46. Ground Admittance near LCC, SLC-6

the predicted ground motion. The resulting "ground motion samples" can then be used to characterize the STS motion environment around the time of maximum loading.

The elastic vibrations expected within the LCC due to launch generated acoustics can be forecast in much the same manner that we have just constructed the ground term. As in the case of ground motion, the key element is the correct representation of the spacial and temporal properties of the acoustic load. A test explosion located above the STS launch pad ..as used to calculate the "impulse response" of a point within the structure when the test and launch generated acoustics have common loading characteristics over the structure (see Figure 47). The vibration excited during a STS launch is then estimated by temporal convolution with the acoustic load anticipated for a STS launch.

The effect of the LCC on ground level motion can be seen by forming the ratio between the LCC motion amplitudes found at ground level with corresponding amplitudes obtained for the ground outside near the LCC (see Figure 48). From Figure 46 it is clear that the exterior ground motion is dominated by an air-coupled wave near 5-8 Hz. In this band the corresponding amplitudes within the LCC at ground level are less than the exterior terms. The structure has the

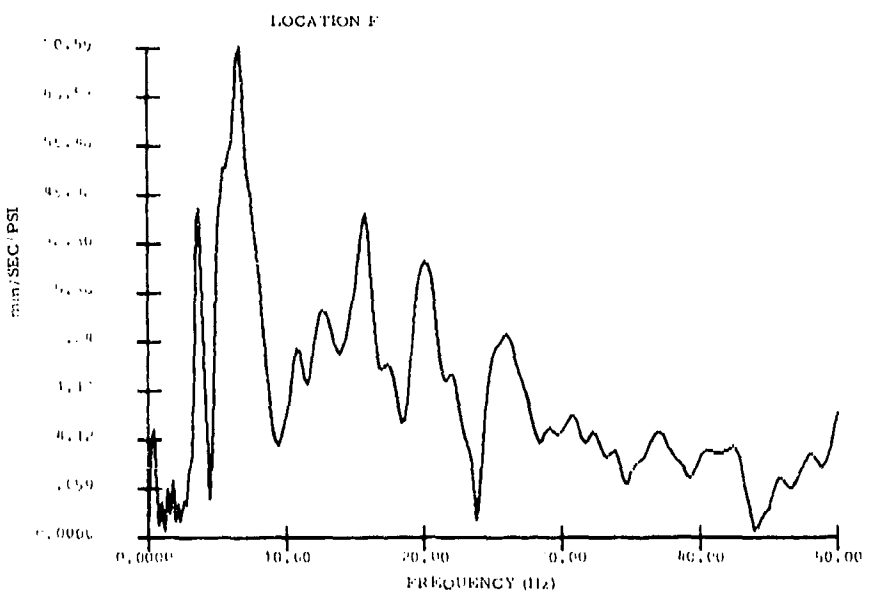


Figure 47. LCC Basement Response

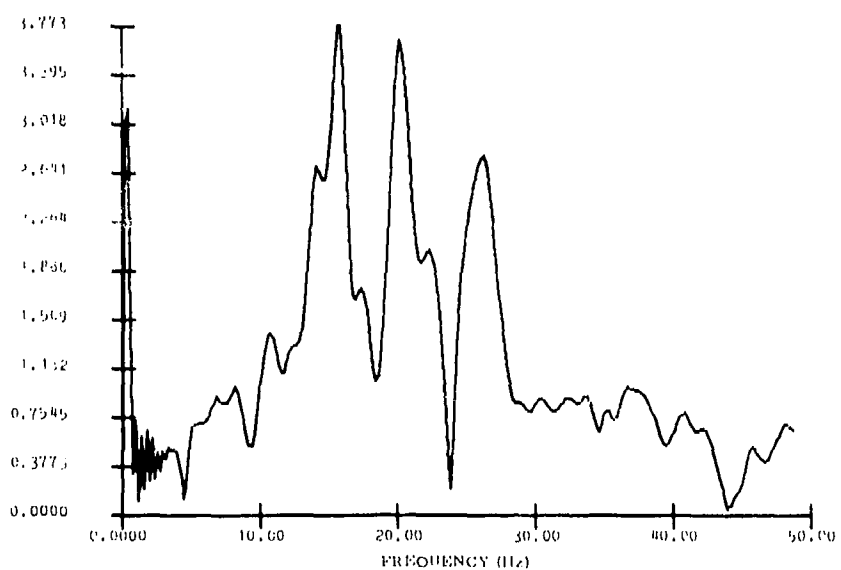


Figure 48. Ground Level Amplitude Ratio: LCC Base Run

effect of attenuating the air-coupled wave. In contrast over the band 12-28 Hz, the building responses clearly dominate. Motion in this band is substantially larger than the corresponding ground levels computed outside.

Where comparisons are possible, motion estimates based on linear elastic, three-dimensional finite element modeling of the LCC moderately overestimates both the level and duration of the basement motion due to seismo-acoustic loads.²⁸ The damping terms selected for modeling the LCC response, while within the range of accepted values, are found to be conservative. It is quite prudent that damping terms be selected conservatively, for structural response to seismic excitation is quite properly a major subject area for research.²⁹

-
28. Yang, R., and Teegarden, W. (1980) Vibro-Acoustic Study, Martin Marietta Report VCR-79-145, Part II.
 29. Simpson, I. (1978) On the interaction of Rayleigh waves with structures, Earthq. Eng. Struct. Dyn. 6:247-263.

References

1. SAMSO/AICL Memorandum of Agreement, dated 31 January 1979.
2. Morse, P., and Feshbach, H. (1953) Methods of Theoretical Physics, Part II, McGraw-Hill, New York.
3. Mickey, W. (1962) Seismic Investigation of Missile Launchings, U.S. Dept. of Commerce, Coast and Geodetic Survey Publication.
4. McCarty, V., and Dalins, I. (1974) Frequency shift in air-coupled surface waves originated by rocket launches, J. Geophys. Res. 76:7027-7039.
5. Haskell, N. (1962) Crustal reflection of P and SV waves, Bull. Seism. Soc. Am. 57:4751-4767.
6. Abo-Zena, A. (1979) Dispersion function computations for unlimited frequency values, Geophys. J.R. Astr. Soc. 58:91-105.
7. Ewing, W., et al (1957) Elastic Waves in a Layered Media, McGraw-Hill, New York.
8. Crowley, F., and Ossing, H. (1969) On the Application of Air-Coupled Seismic Waves, AFCRL-69-0312.
9. Gilbert, F. (1964) Propagation of transient leaking modes in a stratified elastic waveguide, Reviews of Geophysics 3:123-153.
10. Donn, W., et al (1971) Air-coupled seismic waves at long range from Apollo launchings, J. R. Astr. Soc. 26:161-171.
11. Espinosa, A., and Mickey, W. (1968) Observations of coupled seismic waves from sonic booms, a short note, Acustica 20:88-91.
12. Haskell, N. (1951) A note on air-coupled surface waves, Bull. Seism. Soc. Am. 41:295-300.
13. Gubanov, A. (1945) Rayleigh waves on a boundary between a solid and a liquid, J. Exptl. Theoret. Phys. (USSR) 15:497.
14. Blackman, R., and Tukey, W. (1959) The Measurement of Power Spectra, Dover Publications, New York.

15. Hinich, M., and Caly, C. (1968) The application of the discrete Fourier transform in the estimation of power spectra, coherence, and spectra of geophysical data, Reviews of Geophysics 6:347-360.
16. Kimball, B., and Lemon, E. (1970) Spectra of air pressure fluctuations at the soil surface, J. Geophys. Res. 75:6771-6777.
17. Ballard, R. (1970) Dynamic Behavior of Launch Facility Foundation and Surrounding Areas, Miscellaneous Paper S-70-20, U.S. Army Waterways Experimental Station.
18. Oppenheim, A., and Schafer, R. (1975) Digital Signal Processing, Prentice-Hall, N.J.
19. Cole, J. et al (1957) Noise Radiation from Fourteen Types of Rockets in the 1,000 to 130,000 Pounds Thrust Range, WADC Technical Report 57-354 (AD 130794).
20. NASA Report Sp-8072 (1971) Acoustic Loads Generated by the Propulsion System
21. NASA Report GP-1059, Revision A (1976) Environment and Test Specification Levels Ground Support Equipment for Space Shuttle Launch Complex 39:1.
22. Lee, Y. (1960) Statistical Theory of Communication, John Wiley & Sons, N.Y.
23. Owen, D. (1962) Handbook of Statistical Tables, Addison-Wesley Publishing Co., Reading, MA.
24. Powell, A. (1964) Theory of vortex sound, J. Acoust. Soc. Am. 36:177-195.
25. Ywen, C. (1979) On the smooth periodogram method for spectrum estimation, Signal Processing 1:83-86.
26. Hartnett, E., and Carleen, E. (1980) Characterization of Titan III-D Acoustic Pressure Spectra by Least Squares Fit to Theoretical Model, AFGL-TR-80-004.
27. Smith, J., The Aerospace Corporation, Ltr dated 4 January 1980, Rocket Engine Parameters.
28. Yang, R., and Teegarden, W. (1980, Vibro-Acoustic Study, Martin Marietta Report VCR-79-145, Part II.
29. Simpson, I. (1978) On the interaction of Rayleigh waves with structures, Eqrthq. Eng. Struct. Dyn. 6:247-263.

List of Symbols and Abbreviations

c	phase velocity
c_α	phase velocity: air wave
c_R	phase velocity: Rayleigh wave at array offset distance
c_o, U	phase-group velocity for model half space
DOF	degrees of freedom
f	frequency
f_m	maximum spectral frequency
f_n	Nyquist frequency
FFT	Fast Fourier Transform (forward)
FFT^{-1}	Fast Fourier Transform (inverse)
G	Green's function
H	depth
H_s	source height
H_R	rocket height
$H(t)$	measurement system response
M	figure of merit
m_o	mean
n	number of runs
OASPL	overall sound pressure level
OBSPL	octave band sound pressure level
P_{OA}	overall sound power
P_{pp}	pressure power spectral density
P_ϕ	source shaping operation

p_A	pressure amplitude
p'	predicted pressure
p_i	incident pressure
p_r	reflected pressure
p_s	surface pressure
R	source observer distance
r_o	source distance from origin
S_o^2	mean square-reference pressure
T	duration
t	time
t_o	reference time
t_i	i th sample time
v_p	compressed wave velocity
v_s	shear wave velocity
v_z'	particle velocity
v_z	particle velocity estimate
$V_\phi(t)$	ground surface pressure operator
$W(t)$	exhaust power
WOA	overall exhaust power
$Y(c, f)$	acceptance
$Z(c, f, z = 0)$	impedance
*	linear convolution
$\langle \rangle_{\text{sec}}$	time averaging
Δ	offset source distance
Δ_j	offset launch pad distance
Δ_o	reference launch pad distance
δ_o	Dirac delta function
$\delta \Delta_j$	reference point offset
ϵ_j	mean square error - jth
$\epsilon(t_o)$	zero mean, normal, stationary, independent stochastic process
ρ	density
σ	rms of normal process
τ	delay time
$\hat{\tau}$	best delay
ϕ	observer-source elevation angle
ω	angular frequency

Appendix A

Computerized Algorithm for a Layered Whole Space

The method of Abo-Zena⁶ was used to compute the behavior of acoustic waves in a fluid half-space (air) incident on an alluvial layer resting on a half-space of rock (Figure 1).

For each of the media:

$$\mu = -ikb_1 \cosh(r_\alpha kz) - ikb_2 \sinh(r_\alpha kz) - \gamma_\beta kb_3 \sinh(r_\beta kz) \\ - r_\beta kb_4 \cosh(r_\beta kz)$$

$$w = r_\alpha kb_1 \sinh(r_\alpha kz) + r_\alpha kb_2 \cosh(r_\alpha kz) - ikb_3 \cosh(r_\beta kz) \\ - ikb_4 \sinh(r_\beta kz)$$

$$\sigma_z = \rho(\gamma - 1) k^2 c^2 b_1 \cosh(r_\alpha kz) + \rho(\gamma - 1) k^2 c^2 \sinh(r_\alpha kz) \\ - ik^2 r_\beta^2 \mu b_3 \sinh(r_\beta kz) - ir_\beta^2 \mu h^2 b_4 \cosh(r_\beta kz)$$

$$T_{xz} = -2i\rho\beta^2 r_\alpha k^2 b_1 \sinh(r_\alpha kz) - 2ir_\alpha \rho\beta^2 k^2 b_2 \cosh(r_\alpha kz) + (\gamma - 1)\rho k^2 c^2 b_3 \cosh(r_\beta kz) \\ - (\gamma - 1)k^2 c^2 \rho b_4 \sinh(r_\beta kz)$$

where

u = x component of displacement

w = z component of displacement

σ_z = normal stress

T_{xz} = tangential stress

ρ = density

λ, μ = Lamé elastic constants

$$\beta = \sqrt{\frac{\mu}{\rho}}$$

c = phase velocity of free wave along x axis

w = radial frequency

$$k = \frac{w}{c}$$

$$i = \sqrt{-1}$$

$$r_\alpha = \sqrt{1 - \left(\frac{c}{\sigma}\right)^2}$$

$$r_\beta = \sqrt{1 - \left(\frac{c}{\beta}\right)^2}$$

$$\gamma = 2 \left(\frac{\beta}{c}\right)^2$$

$$\alpha = V_p$$

$$\beta = V_s$$

and b_1, b_2, b_3 and b_4 are to be determined for each medium according to boundary conditions.

Using Abo-Zena's method and notation, the system of equations for each layer can be combined:

$$B_2 = U_2(0)^{-1} A_1 U_0(0) B_0$$

where

$$B_0 = \begin{bmatrix} b_1 \\ b_2 \\ ib_3 \\ ib_4 \end{bmatrix} = \text{set of } b\text{'s for top layer (air)}$$

$$B = \begin{bmatrix} b'_1 \\ b'_2 \\ ib'_3 \\ ib'_4 \end{bmatrix} = \text{set of } b\text{'s for bottom layer (rock)}$$

$$U(0) = \begin{bmatrix} 1 & 0 & 0 & r_{\beta_0} \\ 0 & r_{\alpha_0} & 1 & 0 \\ \rho_0(\gamma_0 - 1) & 0 & 0 & \rho_0 \gamma_0 r_{\beta_0} \\ 0 & \rho_0 \gamma_0 r_{\alpha_0} & \rho_0(\gamma_0 - 1) & 0 \end{bmatrix}$$

$$U_2(0)^{-1} = \begin{bmatrix} \gamma_2 & 0 & -\frac{1}{\rho_2} & 0 \\ 0 & -\frac{(\gamma_2 - 1)}{\gamma_{\alpha_2}} & 0 & \frac{1}{\rho_2 r_{\alpha_2}} \\ 0 & \gamma_2 & 0 & -\frac{1}{\rho_2} \\ -\frac{(\gamma_2 - 1)}{r_{\beta_2}} & 0 & \frac{1}{\rho_2 r_{\beta_2}} & 0 \end{bmatrix}$$

and

$$A_1 = \mu_1(h) U_1(0)^{-1}$$

where

$$\mu_1(h) = \begin{bmatrix} \cosh(r_{\alpha_1} kh) & \sinh(r_{\alpha_1} kh) & r_{\beta_1} \sinh(r_{\beta_1} kh) & r_{\beta_1} \cosh(r_{\beta_1} kh) \\ r_{\alpha_1} \sinh(r_{\alpha_1} kh) & r_{\alpha_1} \cosh(r_{\alpha_1} kh) & \cosh(r_{\beta_1} kh) & \sinh(r_{\beta_1} kh) \\ \rho_1(\gamma_1 - 1) \cosh(r_{\alpha_1} kh) & \rho_1(\gamma_1 - 1) \sinh(r_{\alpha_1} kh) & \frac{r_{\beta_1}^2 \mu_1}{c^2} \sinh(r_{\beta_1} kh) & \frac{r_{\beta_1}^2 \mu_1}{c^2} \cosh(r_{\beta_1} kh) \\ \rho_1 \gamma_1 r_{\alpha_1} \sinh(r_{\alpha_1} kh) & \rho_1 \gamma_1 r_{\alpha_1} \cosh(r_{\alpha_1} kh) & \rho_1(\gamma_1 - 1) \cosh(r_{\beta_1} kh) & \rho_1(\gamma_1 - 1) \sinh(r_{\beta_1} kh) \end{bmatrix}$$

and

h = thickness of layer

$$\mu_1(0)^{-1} = \begin{bmatrix} \gamma_1 & 0 & -\frac{1}{\rho_1} & 0 \\ 0 & -\frac{(\gamma_1 - 1)}{r_{\alpha_1}} & 0 & \frac{1}{\rho_1 r_{\alpha_1}} \\ 0 & \gamma_1 & 0 & \frac{1}{\rho_1} \\ -\frac{(\gamma_1 - 1)}{r_{\beta_1}} & 0 & \frac{1}{\rho_1 r_{\beta_1}} & 0 \end{bmatrix}$$

for fluid layer:

$$\beta_0 = 0$$

$$\gamma_0 = 0$$

$$r_{\beta_0} \rightarrow \infty$$

and since this layer is semi-infinite $b_3 = b_4 = 0$ multiplying:

$$\mu_0(0)B_0 = \begin{bmatrix} 1 & 0 & 0 & \infty \\ 0 & r_{\alpha_0} & 1 & 0 \\ -\rho_0 & 0 & 0 & 0 \\ 0 & 0 & -\rho_0 & 0 \end{bmatrix} \quad \begin{bmatrix} b_1 \\ b_2 \\ 0 \\ 0 \end{bmatrix} = \begin{bmatrix} x \\ y_2 \\ y_1 \\ 0 \end{bmatrix}$$

where

$$y_2 = r_{\alpha_0} b_2$$

$$y_1 = -\rho_0 b_1$$

and x is an indefinite term due to the $\infty \cdot 0$ product. Representing the $U_z(0)^{-1}A$ product as

$$C = \begin{bmatrix} c_{11} & c_{12} & c_{13} & c_{14} \\ c_{21} & c_{22} & c_{23} & c_{24} \\ c_{31} & c_{32} & c_{33} & c_{34} \\ c_{41} & c_{42} & c_{43} & c_{44} \end{bmatrix}$$

the equations can be rewritten:

$$B_2 = CY .$$

In the bottom medium, to ensure waves traveling in the positive z direction (no source at $z = \infty$), $b_2^1 = b_1^1$ and $b_4^1 = b_3^1$ therefore,

$$\begin{bmatrix} b_1^1 \\ b_1^1 \\ -jb_3^1 \\ -jb_3^1 \end{bmatrix} = \begin{bmatrix} C \end{bmatrix} \cdot \begin{bmatrix} x \\ y_2 \\ y_1 \\ 0 \end{bmatrix}$$

x can be eliminated and y_2/y_1 solved for:

$$y_2/y_1 = \left| \frac{(c_{41} - c_{31})(c_{13} - c_{23}) + (c_{43} - c_{33})(c_{21} - c_{11})}{(c_{31} - c_{41})(c_{12} - c_{22}) + (c_{32} - c_{42})(c_{21} - c_{11})} \right|$$

and

$$b_2/b_1 = -\rho_0/r_{\alpha_0} \cdot y_2/y_1$$

$$\text{incident wave} = \frac{b_1 + b_2}{2} e^{i(\omega t - kx)}$$

$$\text{reflected wave} = \frac{b_1 - b_2}{2} e^{i(\omega t - kx)}$$

$$\text{incident + reflected} = \text{total} = b_1 e^{i(\omega t - kx)}$$

$$\text{incident} - \text{reflected} = \text{transmitted} = b_2 e^{i(\omega t - kx)}$$

$$\text{ratio of total to incident} = \frac{2b_1}{b_1 + b_2}$$

$$\text{admittance} = \frac{dw/dt/\sigma_z}{-p_0(k^2 c^2) b_1} = \frac{i\omega r k b_2}{-p_0(k^2 c^2) b_1} = \frac{i\alpha_0 b_2}{-p_0 c b_1} = \frac{iy_2}{cy_1} .$$

Appendix B

Inverse Operator

System response was fine tuned by generating theoretical responses, computing inverse FFT's and comparing these with calibration responses. Overall gain, pole location of seismometers, and damping were adjusted until the difference between theoretical and observed was minimized in the least squares sense.

Having generated the theoretical response of the system, the next task was to generate an operator which would yield the input of the system when convolved with its output. To do this, the reciprocal of the magnitude of the response in the frequency domain was computed along with the negative of the phase. To insure that the inverse FFT would be real, a linear function of frequency was added to the phase such that the phase at the Nyquist frequency would be -180 degrees. To reduce the effect of corners, the value of the magnitude at the Nyquist frequency is halved. The inverse FFT was computed using 512 samples. The operator thus produced had enough zeroes to ensure that the convolution could be performed linearly.

To check the performance of the operator, a forward operator was generated by computing the inverse FFT of the system response. This was convolved with a series of random numbers. When the result was convolved with the inverse operator, the series produced had an RMS within 0.1 percent of the original.

Appendix C

Admittance Estimate and Prediction Operator

To estimate the admittance, the pressure and vertical ground velocity at the arrival of the ignition pulse were isolated. Using speed of sound in air, the estimated arrival time was 0.83 sec after ignition. The corresponding channels, corrected for system response, were multiplied by the following factor:

$$f = \begin{cases} 0 & t < 0.3 \\ \frac{1 - \cos(t - 3)/4 + \pi}{2} & 0.3 \leq t < 0.7 \\ 1 & 0.7 \leq t < 2.1 \\ \frac{1 + \cos(t - 2.1)/0.4 + \pi}{2} & 2.1 \leq t < 2.5 \\ 0 & t \geq 2.5 \end{cases}$$

FFT's containing 512 points were computed, and the ratio of amplitude of velocity to amplitude of pressure and difference between phase of velocity and phase of pressure used to generate an operator by computing the inverse FFT. This operator continued nonzero throughout its 5.12 sec length. To eliminate this, it was multiplied by a decaying exponential thus:

$$f = \begin{cases} 0 & t < 0.64 \\ 1.35 e^{-(t-0.64)/0.64} & t \geq 0.64 \end{cases}$$

where the factor of 1.35 is necessary to preserve the mean square of the operator.
The FFT of this operator was defined as the admittance.

Appendix D

Titan III Launch Profile

Table D1. Titan III Launch Profile Values

Simulated t(sec)	Range in ft. (m)	$\log_{10} t$	$\log_{10} R$
1.015	5(1.5)	0.0065	0.6990
1.404	12(3.7)	0.1474	1.0792
1.795	22(6.7)	0.2541	1.3424
2.185	34(10.4)	0.3395	1.5315
2.575	50(15.2)	0.4108	1.6990
2.966	68(20.7)	0.4722	1.8325
3.356	89(27.1)	0.5258	1.9494
3.747	113(34.4)	0.5737	2.0531
4.137	140(42.7)	0.6167	2.1461
4.527	170(51.8)	0.6558	2.2304
4.918	202(61.6)	0.6918	2.3054
5.308	238(72.5)	0.7249	2.3766
6.089	319(97.2)	0.7845	2.5038
6.870	413(125.9)	0.8370	2.6160
7.651	520(158.5)	0.8837	2.7160
8.432	639(194.8)	0.9259	2.8055
9.212	771(235)	0.9644	2.8871
9.993	916(279.2)	0.9997	2.9619
10.774	1075(327.7)	1.0324	3.0314
12.336	1433(436.8)	1.0912	3.1562
13.116			
13.897			
14.678			
15.459	2316(705.9)	1.1892	3.3647
16.240			
17.021			
17.801	3127(953.1)	1.2604	3.4951
18.582			
18.973			
20.144	4071(1241)	1.3041	3.6097

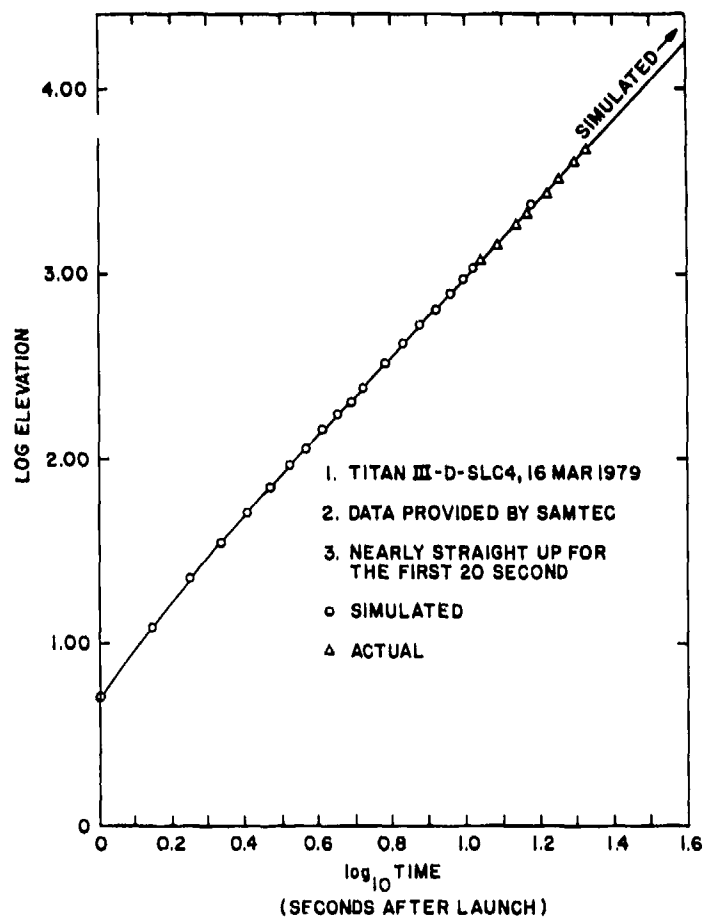


Figure D1. Launch Profile

Appendix E

Phase Velocity and Azimuth Estimate

To compute phase velocity, the phase lags between channels were computed by means of the FFT. To eliminate ambiguities of 2π radians, peak values of each channel were examined around the time of the arrival of the ignition pulse. Samples were dropped from the beginning of each channel, except channel 15 which was closest to the launch point, until all the peaks were aligned and the number of samples dropped from each recorded. Channels were grouped according to distance from each other along the x axis (increasing in west direction).

Channel Pairs	d x separation in ft. (m)	n (relative number of samples dropped)
14-11	20(6.1)	2
11-9	20(6.1)	2
8-14	40(12.2)	4
9-16	40(12.2)	4
15-8	80(24.4)	7
16-13	80(24.4)	7
10-11	0(20(12.2) in y direction)	0
11-12	0(20(12.2) in y direction)	0

Cross spectra were computed using FFT and averaged according to pairing of like distances.

$$X_1(f_k) = 1/2(F_{14}(f_k)F_{11}^*(f_k) + F_{11}(f_k)F_9^*(f_k))$$

$$X_2(f_k) = 1/2(F_8(f_k)F_{14}^*(f_k) + F_9(f_k)F_{16}^*(f_k))$$

$$X_3(f_k) = 1/2(F_{15}(f_k)F_8^*(f_k) + F_{16}(f_k)F_{13}^*(f_k))$$

$$Y(f_k) = 1/2(F_{10}(f_k)F_{11}^*(f_k) + F_{11}(f_k)F_{12}^*(f_k))$$

where for the 256-point transform of data sampled at 100 samples/sec

$$f_k = (k - 1/256) 100 .$$

The phase angles were computed and the phase lag due to the original shifts of n samples restored:

$$\phi_1(f_k) = \tan^{-1}(I_m X_1(f_k)/R_e X_1(f_k)) + 0.01n_1 2\pi f_k$$

$$\phi_2(f_k) = \tan^{-1}(I_m X_2(f_k)/R_e X_2(f_k)) + 0.01n_2 2\pi f_k$$

$$\phi_3(f_k) = \tan^{-1}(I_m X_3(f_k)/R_e X_3(f_k)) + 0.01n_3 2\pi f_k$$

$$\phi_y(f_k) = \tan^{-1}(I_m Y(f_k)/R_e Y(f_k))$$

where $n_1 = 2$, $n_2 = 4$ and $n_3 = 7$.

Phase lags were averaged for a normalized distance of 20 ft. (6.1 m) by

$$\phi(f_k) = 1/3(\phi_x(f_k) + \phi_y(f_k)/2 + \phi_z(f_k)/4)$$

then:

$$\phi_x(f_k) = [\phi_x^2(f_k) + \phi_y^2(f_k)]^{1/2}$$

and:

$$V(f_k) = 2\pi f_k 20/\phi(f_k) = \text{phase velocity}$$

$$\theta(f_k) = \tan^{-1}(\phi_y(f_k)/\phi_x(f_k)) = \text{azimuth angle} .$$

V and θ are computed for each 2.56-sec segment after ignition. As phase velocity increases, the possibility of ambiguity in the phase lag occurs again. Phase angles are monitored, and when they again appear to pass through 2π radians, the number of samples dropped is reduced and n_1 , n_2 , and n_3 updated accordingly.